Microscopy Through Turbid Layers Using Wave Front Shaping

Dissertation

zur

Erlangung der naturwissenschaftlichen Doktorwürde

(Dr. sc. nat.)

vorgelegt der

Mathematisch-naturwissenschaftlichen Fakultät

der

Universität Zürich

von

Giulia Ghielmetti

von

Bellinzona TI

Promotionskomitee

PD Dr. Christof Aegerter (Vorsitz)
Prof. Dr. Hugo Keller
Prof Dr. Frank Scheffold

Zürich, 2014

During this work, nearly by chance, I came across a testimony of one of the great periods of physics. I looked into a paper of Max von Laue, Nobel 1914, professor at our university from 1912 to 1914. Concluding a work on diffraction problems [1], von Laue writes:

Alles dies ist natürlich Folgerung aus der klassischen Wellentheorie des Lichtes, welcher sich in letzter Linie auf die Maxwellschen Gleichungen gründet. Bekanntlich mehren sich in neuerer Zeit die strahlungtheoretischen und quantentheoretischen Bedenken gegen diese Theorie. Dass sich unser Ergebnis an den Versuchen bestätigt, möchten wir darum nicht mit voller Bestimmtheit behaupten. Doch wollen wir, wie schon in der Einleitung gesagt, die Erörterung darüber vertagen, bis weitere Versuche darüber mitgeteilt werden können.

It was a twenty years long period between the quantum and photon hypothesis by Planck and Einstein and the formulation of quantum theory by Heisenberg and Schrödinger. Today we feel that wave optics, electromagnetism and quantum theory are well established theories valid under defined conditions. The words of von Laue show the struggle of mankind to transform artful hypothesis in certainties.

Contents

Abstract

Microscopy through turbid layers is of great interest for biological applications. We present a setup, based on wave front shaping, which allows to image a fluorescent structure behind a turbid layer at diffraction-limited resolution.
In this work we address three main problems. We first propose two methods to create a focus behind a turbid layer: the first based on the direct feedback of a detector placed behind the turbid layer, while the second, without direct access, allows to focus on a fluorescent nanobead. We then show how to move the focus in three dimensions, through memory effect, allowing to obtain an image of the structure behind the turbid layer through the measurement of the fluorescence emitted. Finally we propose an experimental attempt to enhance the contours of the image, based on a second scanning performed with a ring shaped focus.

1 Introduction

Imaging behind turbid structures is of great importance e.g. in applications of biomedical photonics, where often interesting structures are hidden behind turbid layers, such as tissues. Therefore, there have been many attempts to enable the imaging of such structures obscured by turbidity. One prominent way of circumventing this problem has been to discard scattered light with increasing efficiency, e.g. by using confocal microscopy [2] or two-photon microscopy [3]. Multi-photon microscopy has the advantage of using a spectral range of illuminating light where scattering in most biological tissues is less prominent [4]. One drawback is that due to the high photon densities needed to excite multi-photon processes, this needs pulsed laser sources on rather short time scales of tens of femtoseconds. In spite of these great advances, even in the best case of two-photon confocal microscopy, the penetration depth for useful imaging is limited to roughly $500\mu m$, which for many applications is insufficient [3]. An alternative route to the treatment of scattering in imaging applications is to compromise on the spatial resolution that can be obtained while increasing the penetration depth. This is for instance done in optical tomography [5], where using fluorescence contrast, structures deep within a tissue (up to $3cm$) [6] can be resolved, albeit at a reduced resolution of at most a few hundred microns [5, 6].

With the advent of wave-front shaping in extremely turbid media allowing the control of diffusely scattered light [7], either in transmission [8, 9, 10, 11, 12, 13, 14, 15], or in reflection [16, 17, 18] imaging behind or inside turbid media has found renewed interest [19, 20, 21, 22, 23, 24, 25]. There have been several methods proposed, which all rely on the memory effect of multiply scattered light in order to scan the diffuse light behind a layer of turbid material [26, 27, 28]. Initial proposals have created a focus behind the turbid layer, either using direct optical access and wave-front shaping [7] or phase conjugation using second harmonic particles [29], which was then scanned for obtaining an image [20, 22]. There are also other methods which use the scattered light for imaging purpose, by controlling the spatial distribution of the phase of the incoming light [30, 31]. These methods are based on the time-reversal symmetry of the scattering process [32]. This means that a phase conjugated, or temporally reversed field after scattering will make the inverted sequence of scattering, thus leading to a focus at the point of origin of the scattered wave [29]. This has first been intensely

studied using sound waves [33], where a greater degree of control is available and where applications e.g. the destruction of kidney stones are already in use clinically [34]. Another disadvantage is that these methods are invasive, in that they need either some form of optical access for the wave-front optimization or the preparation of second harmonic particles in the sample. Subsequently, the determination of the transmission matrix [35] has been used to transport images through turbid layers [19], however also here optical access is needed to be present. This has been extended recently to focus on structures without direct access by the determination of the singular values of the transmission matrix, which gives access to the diminishingly brighter structures hidden behind the turbid layer [36]. Finally, a computational method based on the memory effect was presented recently, where the wave-front is not adjusted, but the speckle pattern is scanned across a fluorescent structure and the inverse problem is solved to obtain the structure behind the turbid medium [24]. The solution is however not necessarily unique and additional assumptions on the image need to be made in order to find an image.

In order to overcome the necessity of optical access to a direct imaging of fluorescent structures using wave-front shaping, it has been proposed to use the signal of a fluorescent particle for the optimization algorithm and subsequent formation of a focus [20, 37]. This focus would then be scanned to obtain an image of fluorescent structures in the vicinity. The challenge for this proposed technique is that it has only been demonstrated that the solution is unique for a single fluorescent particle. Therefore, one would either need to have a single focusing particle in a structure of different fluorescent particles, albeit with the same absorption properties, or one would have to find a method with which to ensure that even in the presence of several fluorescent particles, only one would have to be used for the focus and the subsequent imaging.

The goal of this work is to make further steps in the creation of a fluorescence based microscope, allowing imaging behind turbid layers without direct access. The main contributions of this work lie in three areas:

1. As first step, we address the challenge of creating a focus behind the turbid layer. We consider two methods. The first one, developed by I. M. Vellekoop, is based on direct light and needs direct access to the sample. The second one [38], derived during this work, allows focusing without direct access to the samples. Our approach works by considering the presence of several fluorescent particles within the sample region, and show that an iteration of an optimization algorithm on the fluorescence signal can be used to focus on the brightest particle, whose surrounding can then be

scanned using the optical memory effect [20, 21]. This iterative technique is based on previous experiments in acoustic waves, where the focusing on scattering structures has been demonstrated as well [39]. Similarly, the method of the transmission matrix described above has similar features [36], where the different iterations in our case correspond to the different singular Eigenvalues of the transmission matrix and thus the different fluorescent particles.

2. Second, we extend the system to be able to scan in three dimensions. In the classic two dimensional case, the focus is scanned around the region of interest using the optical memory effect [27, 28, 26] and a diffraction limited image of the fluorescent structures in the neighborhood is obtained [20]. The scanning is achieved by a tilting of the incoming illumination, which leads to an additional linear phase shift [40]. This phase shift remains correlated during the scattering process over a certain length scale, which then leads to a corresponding shift in the position of the interference focus. However, in the systems shown so far, the imaging is restricted to a single focal plane, which is very hindering for applications. In such applications, the creation of a focus behind a turbid layer relies on a beacon that delivers a contrast that can be detected and increased by wave-front shaping or phase conjugation. This can be a fluorescent particle [37] or a second harmonic generating quantum dot [40]. Thus, by being limited to a single plane of imaging, any interesting structures in the vicinity of the beacon but in a different plane cannot be imaged. Similar to two-photon microscopy, one would therefore like to be able to also investigate the third dimension. Unfortunately it is not possible to simply scan the sample for this purpose, since this will lead to random phase shifts induced by the scattering layer, which destroy the interference based focus. This will already happen for movements on a scale of the wavelength divided by the number of scattering events, i.e. a few nm in our case. We show that this can however be achieved by adding an additional parabolic phase shift to the spatial light modulation. This phase field works as the addition of a lens, which will move the focus in the z-direction. As with the linear phase shift for the planar scanning, the memory effects leads to a conservation of the change in focus over a certain angular range given by the thickness of the turbid layer.

3. The last part of this work is an attempt to improve the quality of the image. The resolution of the result from scanning is obviously limited by

diffraction, and a way to overcome this problem would be of great interest. Many methods to increase the resolution have already been proposed in different fields [41]. We try a simple procedure based on beam shaping which improves the sharpness of the contours and therefore helps distinguishing near points. This method needs to be improved experimentally and further application need to be tested.

This document is organized as follows: in Chapter 2, we discuss the theory and technical details related to this work, discussing the propagation of light through turbid media and how beam shaping can be exploited to focus the scattered light past the turbid layer. In Chapter 3, we present the setup we used in our experiments, discussing the hardware components, the samples, and the software program that controls the experiments. Chapters 4, 5, and 6, addresses the three work packages listed above, creation of a focus, extension of scanning to 3D and improvement of the image quality. Finally, Chapter 7, discusses the outcome and outlook of this work.

2 Theoretical Background

In this chapter, we discuss the theory necessary to address the subjects of this thesis. First, we introduce laser beams and their main characteristics, we discuss what a turbid medium is and, given the nature of our experiments, how it interacts with light. We then explain the concept of beam shaping, which we use to create a focus behind a turbid layer, and finally, we explain the principle we use to move the focus behind the turbid layer, called optical memory effect.

2.1 The laser beam

All the work done in this thesis is based on laser, therefore we obviously need to investigate the properties of a laser beam.

The degree of intrinsic quality of the light is given by the degree of coherence. A light beam is said to be coherent if, for two arbitrary points, one next to the other in the propagation direction, the field oscillates always with the same difference in phase (temporal coherence), and if the same is true for two arbitrary points perpendicular to the propagation direction (spatial coherence).
An example of a wave with ideal coherence is a monochromatic plane wave, which can be easily produced in the radio frequencies through an emitting dipole (far away from the dipole). The oscillation of the electrons in the dipole gives the frequency to the emitted waves.

For light frequencies, the most common sources (i.e. sun, incandescence bulbs), do not produce coherence at all.

Even if we look at a distinct frequency component of these sources, i.e. light produced by energy jumps between two well defined energy levels of well defined atoms, the atoms decay in an absolutely chaotic way, giving rise to a field with completely disordered phase and intensity.

On the other hand, the electric field which gives rise to the decay in the laser cavity induces a decay with high observance of the phase, in such a way to produce waves with phases close to those of plane waves. Actually, in a classical

context the mechanism of the laser can be seen as a field which induces dipoles in the atoms of the cavity and makes them oscillate at a coordinated rhythm. The process of emission in the laser is therefore a collective process. The laser light is a coherent light emitted from a set of coordinated oscillators.

The laser cavity also acts in other positive ways on the quality of the emitted beam. The first one is the accuracy of the induction mechanism which, with the help of the geometry of the cavity, not only gives a perfect order in the phase, but it controls the directionality of the emitted field, allowing particularly thin beams. Actually, all the electrical parameters of the emitted field (frequency, direction, polarization), correspond to those of the inducing field. The accuracy of this process can be explained through the strength of the inducing field which builds up inside the cavity. The very small divergence of the laser beam allows to focus it with high precision, and this is very important for our applications.

Another advantage given by the laser cavity is that a retroactive process, which can be explained by quantum physics, ensures the stability of the intensity of the emitted light. Even this property does not exist in the thermal light, and is of great use for applications.

Besides these excellent properties, laser light obviously cannot be ideal so that the laser line has a width which results from the fact that the phases vary in a random way (phase diffusion) over time, but even in this the laser light is superior to thermal light, where in addition to the phase diffusion, fluctuations of the intensity contribute to enlarge the line width.

Quantum optics also shows that the laser beam supplies photons in a very stable way. For our applications this quality does not have great importance (if not indirectly through the stability of the intensity).

All this allows us to understand the laser as "light antenna". The field in the beam cross section is similar to the one of a plane wave (a sinusoidal oscillation) with a Gaussian distribution of the intensity.

There are many different types of laser, different in laser medium, cavity structure and pumping mechanism. They fields vary in stability of the frequency, in intensity and temporal behavior of the emission (i. e. continued, pulsed).

For our experiment we use a Titanium Sapphire laser with a wavelength of 488 nm and a power of 40 mW.

2.2 Turbid Media

The subject of this thesis being microscopy through turbid media stresses the importance of the interaction of the light with a turbid medium. We define as turbid medium a material where light can not propagate free, but is subject to scattering.

Scattering is the phenomenon where light, going through a material, is repeatedly reflected by its structure. Every portion of light going through the medium will follow a different path, producing a random distribution of the phases and of the direction (though forward direction will be preferred) of the out coming light.

We define as mean free path the mean distance covered by light between two reflections inside a medium. The mean free path gives a measure of the turbidity of the medium.

2.2.1 Propagation of light through a turbid medium

As we said above, light going through a turbid medium is subject to scattering. One consequence of this is that the local phase of a light beam after propagating through a turbid medium is not kept constant, since different portions of light of the beam go through different paths of different lengths.

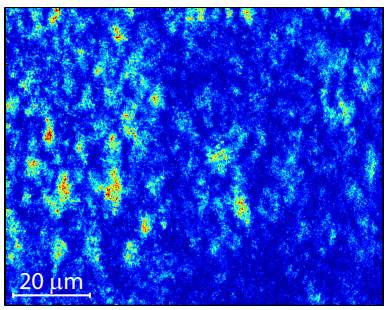

Figure 2.1 – A speckle pattern produced by laser light traveling through a zinc oxide layer of about $15\mu m$.

The light going through different paths, after passing through the medium, interferes and gives rise to a random distribution of the intensity called a speckle pattern (Figure 2.1). Interference obviously occurs only for waves with the same frequency and sufficiently long wave trains, which is the case of a laser beam. A monochromatic beam of thermal light sent through a turbid medium would never produce speckles since the chaotic distribution of the phase of the single

short wave trains of the beam would average away every interference effect. The polarization of the light has also an influence on the result of the interference and hence on the speckle pattern.

For an anisotropic material the speckle pattern created by the light going through the material depends on the region of the material crossed by the light and can therefore not be predicted.

Beam shaping consists of locally modifying the phase and/or the amplitude of a light beam. For this thesis we only shape directly the phase. Phase shaping allows us to play with the interference of different portions of the beam through the phase delays applied to each.

We know that building the focus by phase shaping is what a convex lens does. Let's imagine a laser beam (considered as plane wave) incident perpendicularly on a turbid layer. Since in glass the light has a minor speed than in free space and since by the shape of the lens the paths the light travels across the glass are different from the center to the borders of the lens, the light leaves the lens surface with a radial modulations of the phase. If the shape of the lens is so that the modulated wavefront is an inverse spherical wave, the light proceeds towards a focus. In the language of wave optics we can say that from the lens plane spherical waves are starting with phase differences which produce an inverse spherical wavefront. It is then perfectly clear, that we can imitate a convex lens by an electronic device which modulates the phase.

Now, according to what we said above, if a light beam passes through a turbid medium of reasonable thickness it is submitted to local phase shifts due to the different scattering paths. In the wave optics language spherical waves will start from the lower plane of the turbid medium with a local modifications dependence of the phases, due to the different scattering paths. Thus even if the phases of the single portions of the beam were initially adjusted to converge at a focus, they will no longer do it because of the phase modifications generated by the turbid medium. However if we can readjust the phases with our device and if the thickness and the turbidity of the turbid medium are so, that a change of the phase imposed on the beam portions outside the turbid medium will be conserved when the light passes through the medium, it will not be a problem to recreate a focus.

The device used for beam shaping is called Spatial Light Modulator (SLM).

2.2.2 Relation between the focus profile and speckle statistics

The profile of the focus given by a lens

A focus is built up if a spherical light wave converges towards its center. The ideal focus is a point, but since in practice (e.g. with a lens) we will never produce a spherical light wave but just part of it, the real focus is never a point but has an extension and a profile, described by an Airy function. This is well known. We will nevertheless calculate the profile since we need its explicit form for further considerations.

For simplicity we calculate it in two dimensions. We are looking at the field in a focal plane z = F produced by a plane wave advancing in z-direction and encountering, at z = 0, a slit of dimension 2 R. The situation is shown in Figure 2.2.

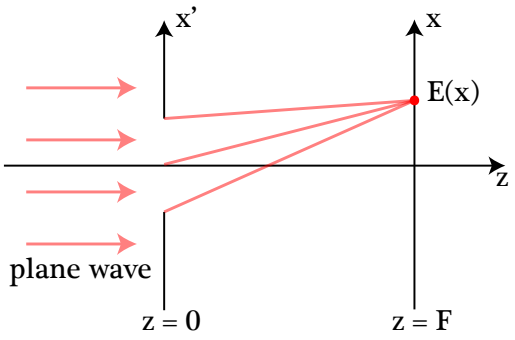

Figure 2.2 – Plane wave passing through a pinhole.

The field in x is given by

$$E(x) = \int_{-R}^{R} dx' \cdot e^{i \cdot k \cdot \sqrt{F^2+(x-x')^2}} \tag{2.1}$$

and, with the paraxial approximation

$$E(x) \approx e^{i \cdot k \cdot F} \cdot \int_{-R}^{R} dx' \cdot e^{i \cdot \frac{k}{2 \cdot F} \cdot (x'-x)^2}. \tag{2.2}$$

Now if at z = 0 we place a lens of focal length F it imprints a quadratic phase of the type $exp\left(\frac{-i \cdot k}{2 \cdot F} \cdot x'^2\right)$ to the field, so we can write the field as

$$\begin{aligned} E(x) &= e^{i\cdot k\cdot F}\cdot\int_{-R}^{R} dx'\cdot e^{-i\cdot\frac{k}{2\cdot F}\cdot x'^2}\cdot e^{i\cdot\frac{k}{2\cdot F}\cdot(x'-x)^2} \\ &= e^{i\cdot k\cdot F}\cdot e^{i\cdot\frac{k}{2\cdot F}\cdot x^2}\cdot\int_{-R}^{R} dx'\cdot e^{i\cdot\frac{k}{F}\cdot x\cdot x'} \\ &= e^{i\cdot k\cdot F}\cdot e^{i\cdot\frac{k}{2\cdot F}\cdot x^2}\cdot A(x) \end{aligned} \tag{2.3}$$

where

$$A(x) = \int_{-R}^{R} dx'\cdot e^{i\cdot\frac{k}{F}\cdot x\cdot x'} \tag{2.4}$$

is the Airy function.

The profile of the intensity is thus given by

$$I(x) = |E(x)|^2 = A^2(x). \tag{2.5}$$

Note that the result is independent of whether the focus is produced by a real lens or by a phase modulator and that it is mainly determined by the width R of the aperture (aberrations). Furthermore, note that if the focus is produced by a phase modulator followed by a turbid medium the scattering in the turbid medium may slightly enlarge the cross-section of the outgoing beam and this reduces the dimension of the focus compared to the case of a classical lens (and increasing R in A(x) makes A(x) sharper).
Calculated for a turbid medium and in three dimensions the result corresponds to equation 2.5 with the Airy function substituted by [43]

$$\mathcal{F}(I_0,\mathbf{r}) = \iint d^2\mathbf{r}'\cdot I_0(\mathbf{r}')\cdot e^{i\cdot\frac{k}{F}\cdot\mathbf{r}'\cdot\Delta\mathbf{r}}. \tag{2.6}$$

The integration is over the back area of the turbid layer and $I_0(\mathbf{r})$ is a kind of intensity averaged over the contributions from the elements of the modulator. $I_0(\mathbf{r})$ thus contains scattering properties and it could annihilate the advantages given by the above mentioned cross section enlargement of the original beam.

Multiple scattering as random field producer

In handling random variables the correlation is a measure of the relationship which may exist between these variables. Statistical variables which are completely independent have no correlation. To define the correlation one takes ensemble averages and sets

$$C(x_1, x_2) \equiv \frac{\langle (I(x_1) - \langle I(x_1)\rangle) \cdot (I(x_2) - \langle I(x_2)\rangle)\rangle}{\langle I(x_1)\rangle \cdot \langle I(x_2)\rangle} = \frac{\langle I(x_1) I(x_2)\rangle}{\langle I(x_1)\rangle \cdot \langle I(x_2)\rangle} - 1. \tag{2.7}$$

The correlation states whether the deviation from their mean value of two random variables are somehow related or not. With this definition, for two independent variables, i. e. for $\langle I(1)I(2)\rangle = \langle I(1)\rangle\langle I(2)\rangle$, one easily verifies that C = 0.

Scattering is a random process. We have stated that light which passes through a turbid medium leaves the medium with a random phase, due to the different paths the single light rays go through because of scattering. On a screen placed behind the turbid medium this fact produces the speckle pattern through the interference of the light portions with different phases. We are thus going to treat multiple scattering in a turbid medium in a model which assumes that multiple scattering produces on the back side of the turbid medium an electric field which is random and which can be described through its spatial auto-correlation function. As a simple approximation, it is quite plausible to take for this auto-correlation function a delta function.

The ensemble averages are formed by taking the average over an adequate number of casually chosen point pairs with distance $x_1 - x_2$ (changing point pairs for a stable speckle pattern or at fixed points with time delay for unstable patterns).

We look at the configuration of Figure 2.2 and imagine that at z = 0 is placed a scatterer which imprints the light with a random phase. For a simple model we set that these phases are uncorrelated

$$\langle S^*(x_1) S(x_2)\rangle = \delta(x_1 - x_2). \tag{2.8}$$

The statistically correct extension of this correlation to four points is

$$\langle S^*(x_1) S^*(x_2) S(x_3) S(x_4)\rangle = \langle S^*(x_1) S(x_3)\rangle\langle S^*(x_2) S(x_4)\rangle + \langle S^*(x_1) S(x_4)\rangle\langle S^*(x_2) S(x_3)\rangle. \tag{2.9}$$

To compute the speckle correlation function C we have to calculate

$$\langle I(x_1) I(x_2)\rangle = \langle E^*(x_1) \cdot E(x_1) E^*(x_2) \cdot E(x_2)\rangle \tag{2.10}$$

and

$$\langle I(x)\rangle = \langle E^*(x)E(x)\rangle. \tag{2.11}$$

With the expression

$$E(x) \approx \exp(i \cdot k \cdot F) \cdot \int_{-R}^{R} dx' \cdot e^{i \cdot \frac{k}{2 \cdot F} \cdot (x-x')^2} \cdot S(x') \tag{2.12}$$

for the electric field the calculation is straight forward and yields

$$\langle I(x_1)I(x_2)\rangle = A^2(x_1 - x_2) + 4 \cdot R^2 \tag{2.13}$$

and

$$\langle I(x)\rangle = 2 \cdot R \tag{2.14}$$

so

$$C(x_1, x_2) = \frac{1}{4 \cdot R^2} \cdot A^2(x_1 - x_2) - 1. \tag{2.15}$$

The correspondence of the shape of the speckle correlation function with that of the focus profile 2.5 is evident.

The calculus in three dimensions [44] again leads to the substitution of the Airy by 2.6 and thus confirms the relation between focus profile and speckle correlation.

The excellent equivalence of the two curves has been measured [43] for several kinds of turbid 'lenses'.

Tough the perfect correspondence of these two curves is often interpreted as an equivalence between the profile of a lens-focus and the auto correlation of the intensities of a random field, it seems absolutely non obvious to find a physical connection between the two phenomena. We feel that the more cautious interpretation merely states that the two phenomena are described by the same mathematical function.

It may be interesting to note that the relation between speckle intensity correlation and focus width has been established by Max von Laue [1] as early as in 1916. Making statistical considerations von Laue has shown that a chaotic field which travels across a circular aperture produces on a screen at a distance F behind the circular aperture a pattern with a chaotic intensity distribution (we would call it a speckle pattern), the correlation length of this intensity distribution being equal to the extension of the focus of a lens with focal length F placed

in the circular aperture. Von Laue considered a chaotic field generated by the diffraction of the field on particles casually distributed in the circular aperture. His calculations are valid in the paraxial approximation.

2.3 Moving a focus in three dimensions through Optical Memory Effect

The theory of the previous sections explains how to build a interference focus, after propagation through a scattering medium. In this section we show that it is possible to move this focus in three dimensions. This is necessary to build a scanning microscope.

2.3.1 Moving a focus in two dimensions

We first look at the scanning in two dimensions, on a x-y plane perpendicular to the direction of the beam. We start from a classical consideration: we know from classical optics, that, if we tilt a beam entering into a transparent medium, the outgoing beam will be shifted (Figure 2.3).

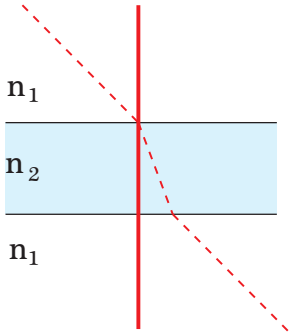

Figure 2.3 – If we tilt a beam going through a medium, his exit point will be shifted.

We therefore analyze the effect of a beam tilting in the case of propagation through a turbid layer.

The situation is shown in Figure 2.4 . To simplify the formulas we address the problem in one dimension. z is the direction of propagation, x' is the coordinate on the upper surface of the turbid layer, while x is the coordinate on the lower

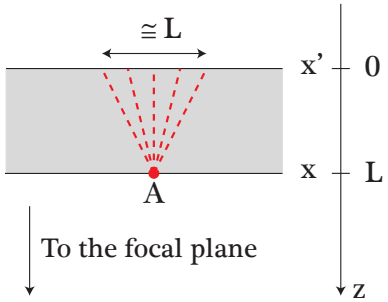

Figure 2.4 – It is reasonable to assume that the light which arrives at a point A of the lower side of the turbid layer without a considerable change of phase comes from a spot of dimension L on the upper side of the turbid layer.

surface. L is the thickness of the turbid layer.

The field after the turbid medium (of thickness L) is given by

$$E_{z=L} = \int dx' \cdot T(x, x') \cdot E_{z=0}(x'). \tag{2.16}$$

The matrix $T(x, x')$ is the transmission matrix of the scattering layer. The field propagates free after the turbid layer. If we observe a focus in a point after the turbid layer, we know that the field leaves the lower surface of the turbid layer towards the focus as a spherical wave and we can conclude that the phases of every beam portion in the plane $E_{z=0}(x')$ are set in such a way that this happens. So

$$E_{z=L} \sim e^{\frac{i \cdot \pi \cdot n \cdot x^2}{\lambda \cdot a}} \tag{2.17}$$

where λ is the wavelength, n is the refractive index of the medium where the light propagates free, and a is its thickness.

We start with a beam perpendicularly incident on the layer. If we tilt the incoming beam by an angle $\Delta\theta = \frac{\Delta k}{k}$, where k is the wave vector $k = \frac{2 \cdot \pi}{\lambda}$ we get an additional phase factor

$$p = e^{i \cdot \Delta k \cdot x'}. \tag{2.18}$$

We make two considerations which permit to predict that this additional phase is transmitted unchanged from the plane z = 0 to the plane z = L giving thus the desired shift of the interference focus. We first assume that points in x' far from x practically do not contribute to the field in the x-plane. It is reasonable to assume a contribution range of extension L. Second we assume that the phase

does not change considerably in the cone of width L. Said otherwise: we state that the linear shift of the focus will only be possible if we tilt the incoming beam with an angle smaller than an amount we are just going to calculate. This second assumption means

$$\begin{aligned} \Delta k \cdot L &< 1 \\ \Delta\theta \cdot k \cdot L &< 1. \end{aligned} \tag{2.19}$$

These conditions give the boundaries for the scanning angle

$$\Delta\theta < \Delta\theta_{max} = \frac{\lambda}{2 \cdot \pi \cdot L}. \tag{2.20}$$

To calculate the shift of the focus corresponding to the angle $\Delta\theta_{max}$ we bring the shifted phase ϕ (from equations 2.17 and 2.18)

$$\phi = \frac{i \cdot \pi}{\lambda} \cdot \left(\frac{n \cdot x^2}{a} + 2 \cdot \Delta\theta \cdot x \right) \tag{2.21}$$

in a quadratic form

$$\begin{aligned} \phi &= \frac{i \cdot \pi}{\lambda} \cdot \left[\frac{n}{a} \cdot \left(x^2 + 2 \cdot \frac{a}{n} \cdot \Delta\theta \right) \right] \\ &= \frac{i \cdot \pi}{\lambda} \cdot \left[\frac{n}{a} \cdot \left(x + \frac{a}{n} \cdot \Delta\theta \right)^2 + R \right] \end{aligned} \tag{2.22}$$

where R does not depend on x.
We see immediately that this yields for the maximum translation in x (Figure 2.5)

$$\Delta f_{max} = \Delta\theta_{max} \cdot \frac{a}{n}. \tag{2.23}$$

We notice that, from the considerations we made, it results that under the same conditions for the tilting, a speckle pattern would be shifted conserving the pattern. This is exactly the phenomenon - experimentally confirmed - which has been explained as due to a memory effect [26, 20]. For our feeling the statement that a phase variation - if it is small - is transmitted because of a memory of the scattering path is perhaps equivalent to the simpler statement that the condition for a phase variation to be transmitted is its being small, or said otherwise: if it seems surprising that in a stochastic process as a multiple scattering there is some continuity, called intuitively memory, it would perhaps not hurt less our intuition, if even the smallest variation of the incident angle would at once produce a drastic variation . The condition for θ_{max} we derived above has first been

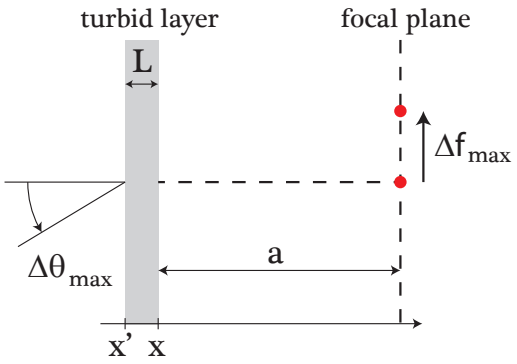

Figure 2.5 – A variation of the angle of incidence $\Delta\theta$ produces a shift of the focus Δf.

obtained from general considerations of correlations and fluctuations of coherent wave transmission through disordered media [26] for scattering samples illuminated by plane waves and then for samples illuminate by a shaped wavefront [20].

2.3.2 Moving a focus along the z axis

We try to achieve the scanning with the focus in three dimensions. This means that in the formula 2.17 for the spherical wave leaving the lower side of the turbid layer we must substitute a by $a + \Delta a$. This again leads to an additional phase of the form

$$\begin{aligned}\Delta\theta = e^{i\cdot\pi\cdot n\cdot\frac{x^2}{\lambda\cdot(a+\Delta a)}-i\cdot\pi\cdot n\cdot\frac{x^2}{\lambda\cdot a}} \\ = e^{i\cdot\pi\cdot n\cdot\frac{x^2}{\lambda\cdot a}\cdot\frac{-\Delta a}{a+\Delta a}} \\ \sim e^{-i\cdot\pi\cdot n\cdot\frac{x^2\cdot\Delta a}{\lambda\cdot a^2}}.\end{aligned} \tag{2.24}$$

We would like to add this additional phase to the field on the upper side of the turbid medium, hoping that then is passes unchanged to the lower side of the turbid medium.

So, let's estimate the range of Δa over which the conservation of the additional phase through the turbid medium is supposed to be possible, condition we have seen to be fundamental for the memory effect. Again, we assume:
- that the light joining to a point x is confined to a cone with a width corresponding to the thickness of the medium.
- and that there is a small variation of phase over the whole basis of this cone for every point of the entire cross section of the light beam.

If we denote by r the radius of the light beam, we have, with 2.24

$$\pi \cdot n \cdot \left[(r+L)^2 - r^2\right] \cdot \frac{|\Delta a|}{\lambda \cdot a^2} \sim \pi \cdot n \cdot 2 \cdot r \cdot L \cdot \frac{|\Delta a|}{\lambda \cdot a^2} < 1. \tag{2.25}$$

This gives the maximum shift Δa_{max}

$$\Delta a_{max} = \frac{\lambda \cdot a^2}{2 \cdot \pi \cdot n \cdot r \cdot L}. \tag{2.26}$$

From equation 2.23 and 2.26 we easily conclude that the memory effect does not work for thick turbid layers.

3 Setup and Technical Details

In this chapter we approach the technical part of this work. This is of main importance for people interested in building a setup for further research in this field.

The basic setup used for the experiments shown in the next chapters is quite complex and needs some particular calibration processes. In the next sections we show and explain in detail the basic setup, we present the main devices used to create a focus and perform the scanning, meaning the spatial light modulator and the galvanometer scanner, we spend some words about the calibration of the setup, and we explain how our samples were built and what are their characteristics.

The experiments are controlled by a PC. Specific software has been developed in Python and C++. At the end of this chapter we give an overview about how this software works and how it interacts with the main elements of the setup.

3.1 Basic setup

The main part of the setup was the same for every experiment. In the chapter corresponding to each experiment we will describe the exact configuration used for the experiment.

Figure 3.1 is a schematic representation of the setup. The laser beam (Spectra-Physics Cyan 40 mW, 488 nm) goes through a beam expander, passes through the galvanometer scanning mirrors (General Scanning LDS-07-OH), is horizontally polarized by the beam splitter 1 and sent on the SLM display (Holoeye HEO 1080 P).

The diameter of the cross section of the beam is as big as the SLM display. On the SLM a region of interest corresponding to the dimension of the beam cross section is set, so that not illuminated pixel are not used. This helps in saving time during the experiments.

The light reflected by the SLM is sent through a beam splitter oriented in such a

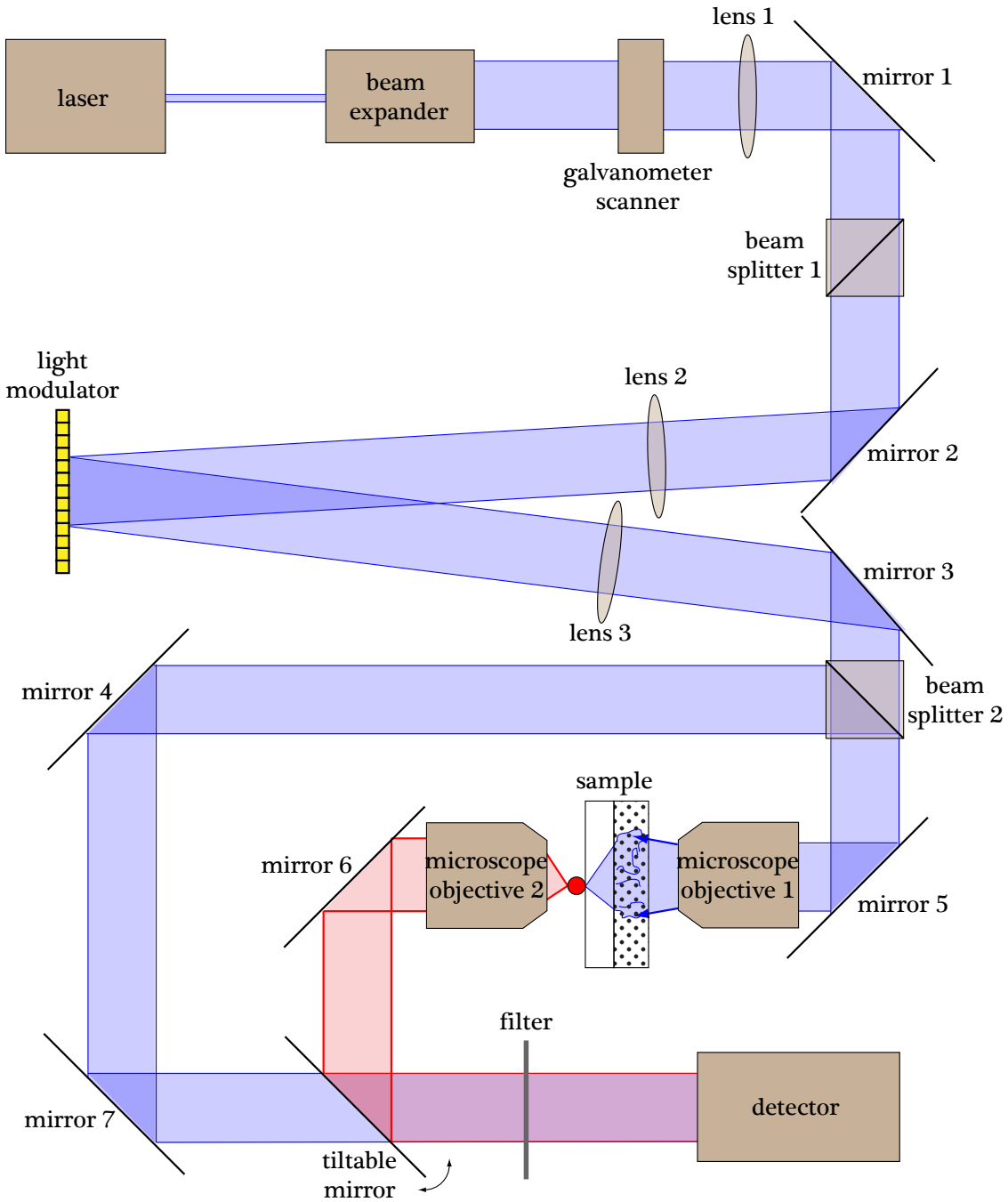

Figure 3.1 – A schematic representation of the basic setup.

way that the light coming from the SLM goes straight through it, but the light coming in the opposite direction is partially reflected with a 90 degrees angle. After passing through the beam splitter, the light is focused on the sample through a microscope objective (Zeiss A-Plan 40x/0.25). A second microscope objective (Zeiss MplanFLN 50x/0.80) focuses on the back surface of the sample. The light goes then on the detector.

The filter is needed to look at the fluorescence. It filters the direct light of the laser.

As a detector we use a CCD camera (AVT Stingray F-145B) or a photomultiplier (Hamamatsu), depending on the experiment.

The beam splitter 2 is used for the adjustment of the first microscope objective, which is done by looking at the light reflected on the surface of the sample, sent to the detector by the mirrors 4 and 7. To be able to switch from the light going through the sample to the light reflected on his surface, the mirror before the detector can be tilted in such a way that it gives free the way for the light reflected on the sample surface and stops the light passed through the sample.

3.1.1 Focusing on the sample

The two microscope objectives have to be adjusted in such a way that the first one images the SLM display on the front surface of the sample, while the second one images the back surface of the sample on the camera.

The sample we used for most of the experiments was a piece of glass between $1mm$ and $2mm$ thick, with a turbid front surface and fluorescent beads, of different dimensions and colors depending on the experiment, on the back.

The first objective is adjusted by loading a diffraction grating with a pattern on the SLM (as shown in Figure 3.2) and looking at the reflection of the zero order on the sample surface with the CCD camera. To look at the light reflected by the front surface of the sample, it is necessary to tilt the mirror before the detector (Figure 3.1). The sample is mounted on a sliding stage, so that it can be shifted until the image of the pattern on the camera looks sharp.

The second objective is adjusted by looking at the light passing through the sample. As a reference we draw some black lines on the back of the sample, so that, while moving the second objective - which is also mounted on a sliding stage - we can see that we are focusing on the sample's back surface if the edges of

the black lines look sharp. It is important that the second objective is adjusted within a range comparable to the diameter of the beads one would like to detect.

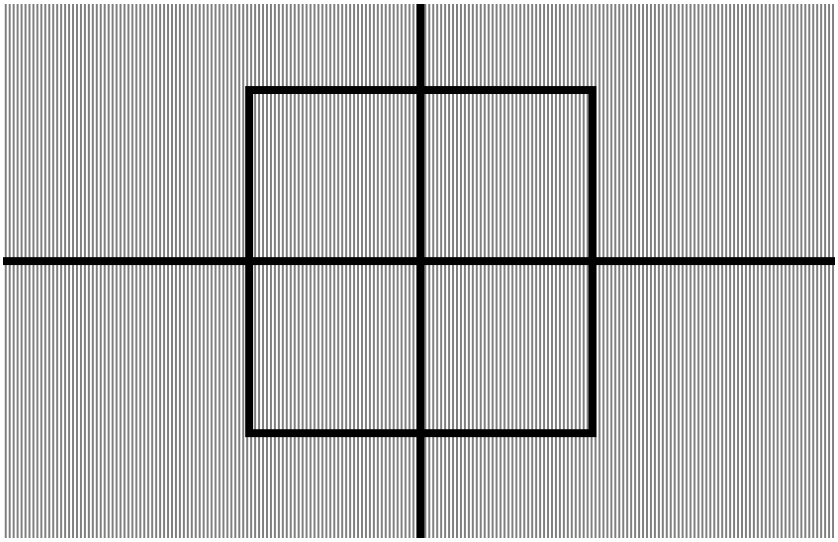

Figure 3.2 – The pattern used for the calibration of the first objective focusing on the sample.

3.2 Setup components

In this section we describe two important components of the setup.

The first one is the galvanometer scanning device. It is composed by two mirrors which can be oriented by a motor and we use it for the scanning on the $x - y$ plane described in chapter 5

The second one is the spatial light modulator, a device which allows to locally modify the phase of a laser beam. We use it for many applications in our experiments, as described in the next chapters.

3.2.1 Galvanometer scanner

The galvanometer scanner consists in two mirrors that can turn perpendicularly and are independent one from the other. The light beam passing through the device is reflected by both mirrors. This allows to move a beam on a plane.

The operating principle of a galvanometer consists in transforming an electrical current into a magnetic moment. The two mirrors are fixed on two coils placed in two constant magnetic fields. When an electrical current, produced by an applied voltage, flows through the coil, a magnetic field is produced. At this point obviously the coil will turn in the given constant magnetic field by an amount corresponding to the strength of the electrical current flowing through it. Hence the orientations of the mirrors and the direction of the light beam can be changed by changing the voltages applied to the two coils.

Our galvanometer scanner (General Scanning LDS-07-OH) allows a maximum angle of ± 22 degrees.

Calibration

The orientation of the scanning mirrors is changed while applying different voltages through a PC.

The calibration of the mirrors, meaning the operation of orienting them in such a way that the laser beam goes straight through the device and the next components of the setup is done "manually", by varying the voltage applied to each mirror by small steps, until the light goes through the correct path.

The voltages corresponding to the correct position of the mirrors are set as default offset in the software which performs the experiments.

3.2.2 Spatial Light Modulator

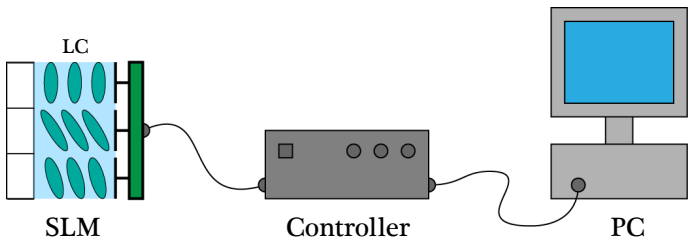

Figure 3.3 – The Spatial Light Modulator is composed by a liquid crystals display. The orientation of the liquid crystals can be changed through an applied voltage and it affects the polarization of the reflected light. The SLM is driven by a PC, through a controller.

There are several types of spatial light modulators, based on different technologies. For our experiments we used a phase only modulator from Holoeye (HEO

1080 P), based on liquid crystals.

This modulator consists of a nematic liquid crystals display connected to a controller and a computer, which allows to pilot the behavior of every modulator pixel. With behavior we mean the modulation of the phase of the light reflected by this point. A light beam reflected by the display thus undergoes a local modulation of phase, which means that every point of the cross-section of the reflected beam has a phase governed by the display. The display measures 15.36x8.64mm^2, corresponding to 1920x1080 pixels.

Each pixel can be controlled individually, but we always used blocs of pixel with a dimension depending on the application. Controlling single pixel decreases the precision of the spatial light modulator, since the value of a pixel affects the value of his neighbor.

The liquid crystals (Figure 3.3) are an anisotropic medium, meaning they have an orientation which, as well as the orientation of their optical axis, depends on an a voltage that can be applied and controlled thorough a computer.

The phase shift given from each pixel to the incident light is influenced by the orientation of the polarization of the incident light with respect to the optical axis of the liquid crystals. Light entering in an anisotropic medium, is split in two components whose electric fields are orthogonal, one of them being orthogonal to the optical axis of the medium.

The two components travel through the medium with different velocities (this effect is known as birefringence) so that, when the two components are recomposed, at the end of the medium, they will oscillate out of phase with respect to each other. This results in a different state of polarization of the reflected light. Figure 3.4 shows an example of how linear polarized light could for instance be transformed in circular polarized light.

Our SLM can work with a maximal frequency of 60 Hz.

Calibration

The SLM has to be calibrated in such a way that by going from 0 to 255 with the greyscale values the phase changes from 0 to 2π.

There are two ways of calibrating the device: using a program from the supplier and a given calibration curve, or using a software written by I. M. Vellekoop

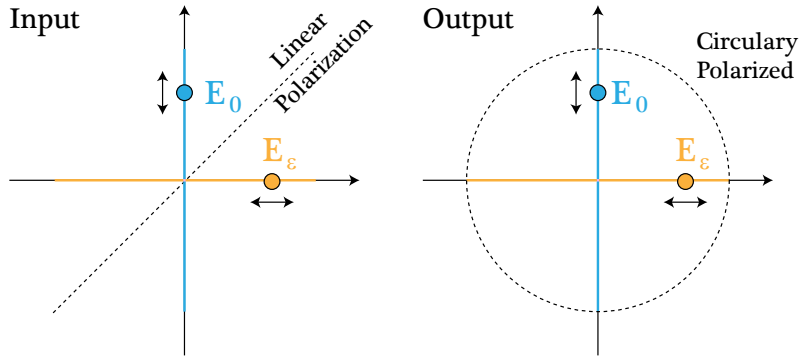

Figure 3.4 – Light modulation: on the left the fields E_0 and E_ϵ are oscillating in phase thus producing a 45° linear polarization; on the right a phase difference of $\frac{\pi}{2}$ gives a circular polarization.

which allows more precision since the curve is directly measured and therefore perfectly adapted to the wavelength of the used laser, $488nm$ in our case.

The principle is the same for the two methods: the liquid crystals allows a maximal phase shift that generally goes above the 2π. The calibration curve is created by measuring the phase shift corresponding to each greyscale value and then "stretching" the voltages corresponding to a 2π phase shift on the values from 0 to 255.

3.3 The samples

As already mentioned, most of the samples we used for the experiments consists in a piece of glass with a thickness of $1mm$ or $2mm$ with a turbid substrate on one side and fluorescent silicon nanobeads on the other.

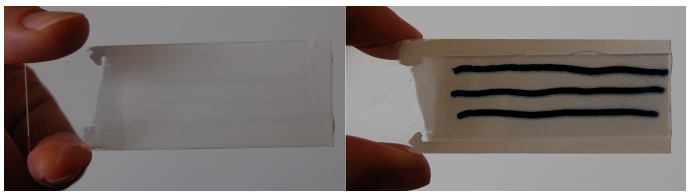

Figure 3.5 – The front side of the $1mm$ sample is covered by a zinc oxide substrate, while on the back there are fluorescent nanobeads (which can obviously not be seen by eye. The black lines are used for adjusting the second objective, as explained in section 3.1.1.)

The turbid substrate of the $1mm$ sample consists of a zinc oxide coat (Figure 3.5), while the $2mm$ sample is a diffuser glass. The zinc oxide coat is created as follows: zinc oxide is diluted in ethanol where glass is immersed quickly. Letting dry the glass horizontally allows to obtain a substrate with uniform thickness of about $15\mu m$. Before the immersion we cover the back surface of the sample with a piece of tape to avoid to have the turbid layer on both sides.

For some of our experiments we used a diffuser glass ($2mm$ sample), shown in Figure 3.6, instead of the glass with the zinc oxide substrate. The sample has a 6 mm thick diffusing 1500 grit polished side.

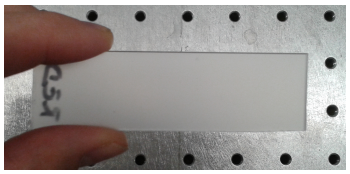

Figure 3.6 – The 2 mm sample consists in a diffuser glass. The nanobeads are applied on the back in the same way as for the 1 mm sample.

We use two different kinds of nanobeads: the first ones have a diameter of 200 nm, have their maximum of emission in the green (508 nm) and the peak of the excitation spectrum at 468 nm; the second ones have a diameter of 450 nm, have their maximum of emission in the red (530 nm) and the peak of the excitation spectrum at 480 nm.

The nanobeads are applied on the back of the sample by diluting them in deionized water with a proportion of 10 μl to 230 ml and spreading uniformly a droplet on the glass until it is completely dry. It is important to spread it accurately to avoid clusters of beads.

After applying the nanobeads, we draw some black lines on the back of the sample (Figure 3.5), which are needed to simplify the process of adjusting the second objective, as explained in section 3.1.1.

Figure 3.7 shows a picture of the nanobeads taken with a confocal microscope, looking at the back of the sample (a) and a picture of the fluorescent signal going through the turbid layer (b). As expected, from panel (b) it is not possible to recognize the nanobeads.

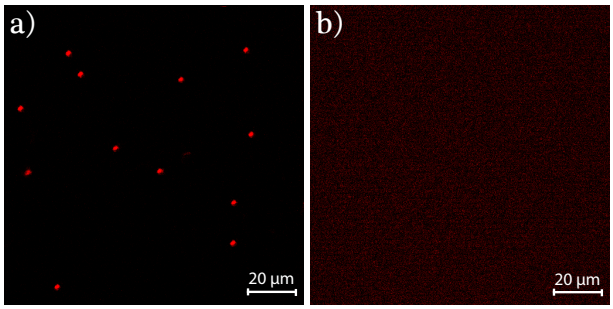

Figure 3.7 – Panel a) shows a picture of the nanobeads taken with a confocal microscope from the back of the sample, while panel b) shows the signal coming through the turbid layer.

3.4 Setup controlling through PC

3.4.1 Overview

To facilitate the experiments, a computer system made of hardware and software was engineered. The software was built targeting modularity, i.e. to allowing the reuse of components, and facilitating future extension. The software was originally developed by Dr. I. M. Vellekoop and extended during this work. The development environment was Microsoft Windows, and the programming languages used are Python and $C++$.

In this Section we discuss a few important concepts which are at the core of the design of our system.

The first important definition is the one of **Component**. The lab computer has been configured so that all the principal hardware devices of the setup (meaning the galvanometer scanner, the SLM, and the detectors) are recognized within the computer as so called components. At the low level, a component consists of the device hardware, its connection to the computer, and the driver program which guide the basic hardware communication, allowing for instance to send commands to the device and read information. At a higher level, each component is handled by a software library, providing functionalities for the general use of the device. For example, given the GalvoScan device, the controlling library has functions for moving the mirrors within a particular range and hence perform a scan of an area. While most devices are connected directly to the motherboard of the computer and exploit the CPU for any computation, the SLM is connected to the graphics card and is recognized as second screen. The computer has no notion of the SLM being different from a traditional computer screen.

The operating system allows the use of Microsoft DirectX to draw on a screen. This is a convenient choice, as DirectX is a flexible library designed for high performances. DirectX also allows to take advangage of the graphics card processor, the GPU, which for certain operations is much faster than the computer CPU. In our system, we take advantage of this to perform per pixel operations directly in the GPU memory, avoiding a costly copy of the data back and forth to the main computer memory, and exploiting the parallelism of the GPU pipelines.

The second definition is the one of **Experiment**. Lab experiments may vary greatly in their use of the hardware, on the computation performed on the computer, and on the time necessary to complete. However, there is a number of properties common to any experiment, such as the need for displaying information to the user and possibly ask for user input, the need to save the results data, etc.. These common properties have been abstracted into a set of classes, again with modularity in mind.

The third definition is the one of **Algorithm**. While the word algorithm has a very broad meaning in Mathematics and Computer Science, in our setup, we specifically focused on algorithms for altering the liquid crystals of the SLM in order to obtain a maximum response, which may be measured with the camera or the photomultiplier. Here modularity comes to great help. We abstracted the fact that any algorithm of this type will operate on the SLM, which we call modulator, and measure the response with a detector. The actual detector being used (camera or photomultiplier) is defined in the actual experiment. Similarly, any pixel operation that may be needed for altering the liquid crystal of the SLM, can be written as pixel shader associated with the modulator component. A variety of experiments can be performed by just altering these parameters while keeping the same core structure of the system.

One important aspect of the algorithms used in this work is the use of a multiscale approach to improve speed. Imagine the following. An algorithm has to decide what grayscale value to assign to each pixel of the SLM on the base of a measured response from a detector. The SLM has a resolution of 1920x1080 pixel. Since each pixel is independent, to find the optimal SLM configuration, the algorithm should test sequentially every single pixel. Depending on the duration of the measurements, this may quickly become prohibitive. Additionally, the change of color of a single pixel may produce a variation of the measured intensity below the noise threshold, making it impossible for the algorithm to make any guess.

Instead, our algorithms work with segments of pixels, where all pixels inside are

treated as one. This addresses the two problems we just mentioned. First it greatly reduces the number of measurements - and hence the time - necessary for the optimization to converge. Second, a segment of pixels changing at once has a higher chance of producing measurable changes, as the portion of the laser beam which changes phase is larger. In our experiments, we saw the benefits of first launching the optimization algorithm with a coarse resolution (7x7 segments), and then refine the optimization increasing the resolution. The first coarse step is important as it increases the intensity in the region of interest. This makes it possible for the algorithm to optimize smaller segments, as the signal to noise ratio is much higher. An example of this can be seen in Figure 4.8.

3.4.2 Program Control Structure

In this section we discuss the structure of the control program more in details. Figure 3.8 shows the class structure for the control program for the experiments discussed in Chapters 4 and 5. Only the most important classes are shown.

The orange boxes on the left show the python class hierarchy created to describe the experiments. The class **LabControl.Experiment** describes a generic experiment, utilizing the UI features provided by the **Tkinter** library to display a window with a user interface as shown in Figure 4.2. The class **RunAlgorithmExperiment** is specialized for handling the execution of an optimization algorithm. By deriving from this class, we can create a specific experiment, linking it to the desired detector and modulator.

The white boxes in the middle show the $C++$ class hierarchy to describe the algorithm. The class **AlgorithmVaryPhase** provide functionalities to change the grayscale value on the SLM, hence producing a change of phase on the light reflecting on it. The class **AlgorithmBlockPhase** further defines the algorithm to utilize the block.

The white boxes on the right show the $C++$ class hierarchy describing the modulator, i.e. the object controlling the SLM. The classes **ModulatorImpl** and **ModulatorDX** deals with creating the DirectX element for displaying grayscale values on the SLM. The class **MDXBitmapBase** adds the support for associating an external image (bitmap) to the grayscale values displayed on the SLM. Finally, the class **MDXFresnelModulator** implements the necessary operations to apply the equivalent of a Fresnel lens by applying the lens data contained in an image on top of the SLM grayscale values altered by the optimization algorithm. Refer to Section 5.2 for further details.

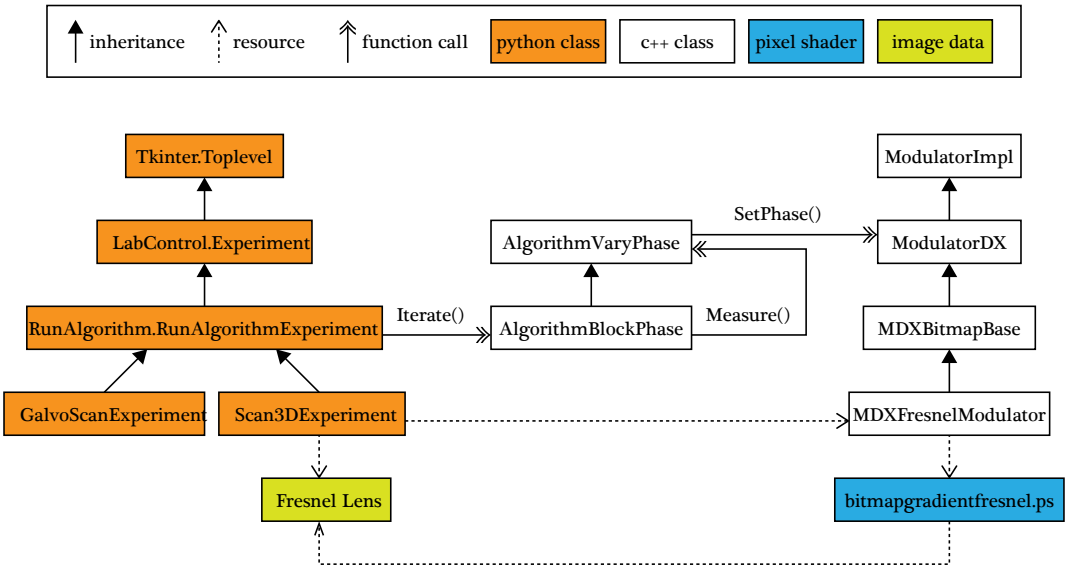

Figure 3.8 – Control Program Structure for running experiments in our system. At high-level, an experiment is written by inheriting from the existing set of python classes, which provide all generic functionalities related to running experiments. When launched, the control program invokes the $C++$ routines which deal with the optimization algorithm (middle) and the alteration of the content displayed on the SLM (right). Specific needs, such as the application of a Fresnel lens in the Scan3DExperiment, are obtained by further specifying the python classes and possibly adding new $C++$ components, such as the case for the **MDXFresnelModulator** class. All experiments in this work are based on the same underlying structure.

4 Creating a focus behind a turbid layer

In this section we show two methods to create a focus behind a turbid layer. The first one is based on a direct feedback from a camera behind the turbid layer, the second one allows to create a focus on a fluorescent nanobead without being invasive.

Being able to create a focus behind a turbid layer is the first step to create a fluorescence microscope.

4.1 Creating a focus through a direct feedback

The first method we propose to create a focus behind a turbid layer consist in locally modifying the phase of the incoming beam through the SLM, in such a way that the intensity of the light on a point behind the layer is maximized. The advantage of this method is the rapidity, the disadvantage is that direct access to the sample is required to measure the signal which is then directly given as feedback. Obviously direct access is for most of the applications a big drawback.

4.1.1 Setup and samples

A schematic representation of the experiment's setup is shown in Figure 4.1. The laser beam goes through a beam expander so that his diameter is adapted to the dimension of the SLM display. We call the portion of the SLM illuminated by the beam Region Of Interest (ROI). After being reflected by the SLM, the beam is focused on the surface of the sample through a 40x microscope objective creating there a spot of a diameter of 80 μm.

The sample consists in a $1mm$ thick glass with a substrate of approximately $15\mu m$ of Zinc Oxide pigment on one side, corresponding to more than 15 mean free paths.

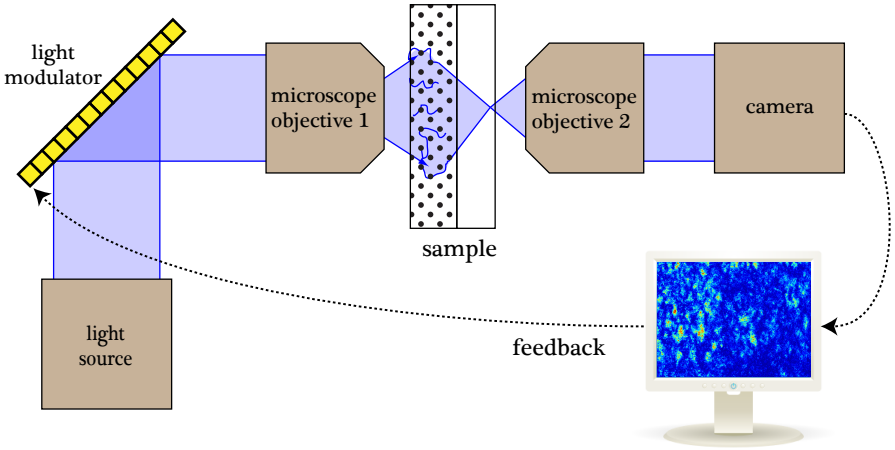

Figure 4.1 – A schematic representation of the setup.

The light behind this layer is highly disordered and has undergone at least 200 scattering events. Thus, the layer is completely nontransparent.

The back side of the sample is imaged on a CCD camera, which gives the feedback signal used for the optimization. With optimization we mean the process of maximizing the light reaching a point behind the turbid layer, which is the process which leads to the creation of the focus.

4.1.2 The optimization algorithm

The basic idea of the iteration process which creates the focus is the following:

1. One divides the beam in a considerable number of equal beam portions (we will start with 7x7).

2. One considers that every beam portion after passing through the turbid medium acquires its own phase shift.

3. The light arriving at the point chosen for the focus, which is the superposition of all the beam portions, let's call it the SUM, is surely not a sinus-wave, but it has the frequency and the period of the beam.

4. One assumes, that if one cancels one of the portions of the SUM, the period of the SUM is not significantly shifted.

5. One changes the phase of one beam portion, looking for an intensity maximum of the superposition of this portion with the SUM (more precisely SUM minus this portion, but see 4.).

6. One knows that at the maximum the considered portion is perfectly in phase with the SUM.

7. One can repeat this procedure for every portion and, because of 4., in this way all the portions are brought in phase and hence produce the desired interference maximum.

This procedure is executed by an optimization algorithm. The algorithm works in two steps which are equivalent in the execution but not in the number of segments in which the SLM is divided. The first step consist in an iteration of the algorithm with bigger segments on the SLM and is needed to get a signal high enough to be processed a second time with smaller segments. As shown by [] , the enhancement of the intensity of the focus is proportional to the number of segments.

The first iteration of the algorithm consists in dividing the SLM ROI in 7x7 segments of 123x123 pixel each. The algorithm goes through all the segments one after the other, and performs every time the following measurement: it assigns five greyscale values equally distributed between 0 and 255 corresponding to five different phase delays to the segment, for each value the intensity of the light, at the position where the focus is desired, is measured. The five intensities are plotted versus the corresponding greyscale values. The point are fitted with a sinus and the greyscale value corresponding to the maximum of the curve is selected for the segment. This process corresponds to align the phases of all the portions of the beam, which means put all the portions of the beam in phase at the position where the focus is desired.

After going through all the segments, the chosen greyscale values are assigned. This creates an increase of the intensity of the light at the position of the focus. At this point it is possible to proceed with a second iteration whit smaller segments.

For our experiment the second iteration was performed with 32x32 segments of 27x27 pixel.

Once the algorithm has finished we obtain a focus at the desired position.

Figure 4.2 shows the user interface of the software which creates the focus. The panel "Camera" shows the current image on the region of interest of the camera, meaning where we create the focus. We set the region of interest in the center of the camera picture. Obviously it would be possible to create the focus even at a

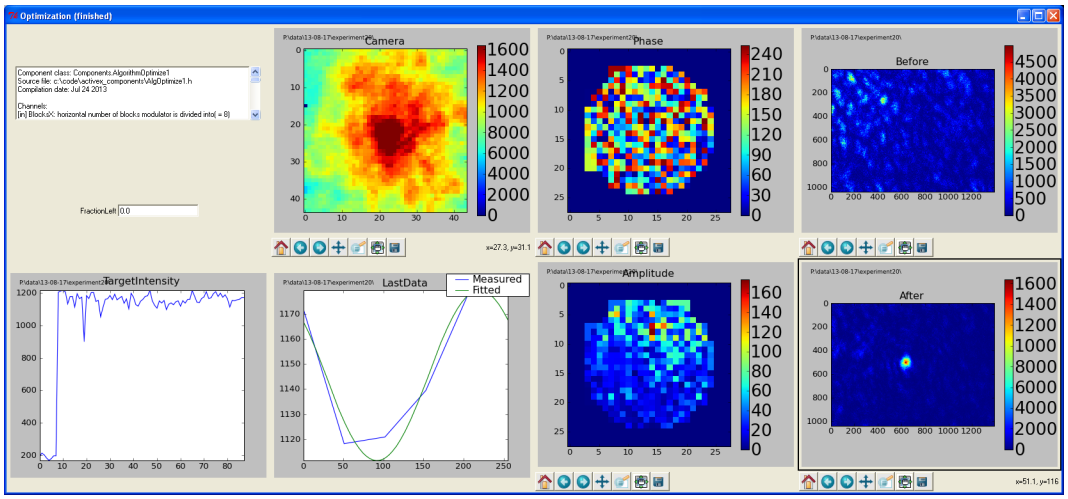

Figure 4.2 – The user interface of the software that creates the focus. "Camera" shows the current image on the region of interest of the camera, "TargetIntensity" shows a curve of the intensity of the region of interest at each step of the algorithm, "LastData" shows the last five measured points fitted by a sinus, "Phase" shows the phase modulation of the SLM, "Amplitude" the corresponding changes in amplitude, and "Before" and "After" show the wholes camera pictures before and after the optimization process.

different position. "TargetIntensity" shows a curve of the intensity of the region of interest every 5 steps of the algorithm. The jump in the curve corresponds to the transition from the first to the second iteration of the algorithm: after the first iteration, the values are set on the SLM and this leads to an enhancement of the intensity at the position of the focus. "LastData" shows the five points corresponding to the measurement of the last segment with the five different greyscale values. the measured points are fitted with a sinus. "Phase" shows the phase modulation of the SLM and "Amplitude" the corresponding changes in amplitude. "Before" and "After" show the whole camera pictures before and after the optimization process.

4.1.3 Experimental results

This experiment has first been performed by I. M. Vellekoop.

Figure 4.3 shows the speckle pattern generated by the laser beam going through the turbid medium, and the focus obtained after the optimization process.

As already mentioned, the enhancement of the intensity of the light is propor-

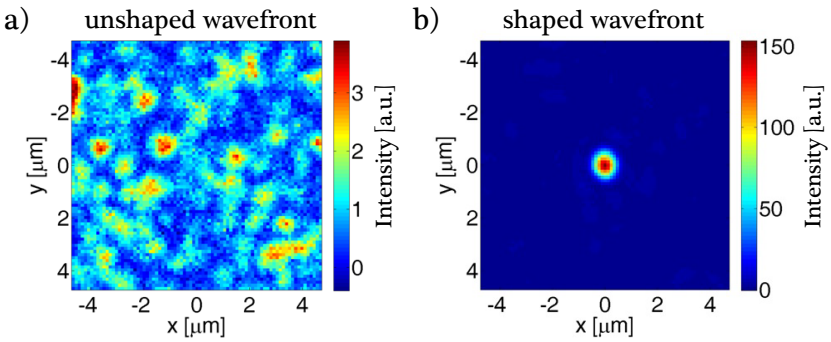

Figure 4.3 – This measurement has been done by I. M. Vellekoop. Panel a) shows the unshaped wavefront while panel b) shows the focus obtained after an optimization with 32x32 segments on the SLM.

tional to the number of segments. With 32x32 segments we obtain a focus 100 times more intense than the background. As we will show in the next chapter, this is good enough to allow scanning of fluorescent structures.

It would for sure be possible to increase the intensity of the focus by increasing the number of segments. To do this a third iteration of the algorithm would be needed, since if the segments are very small, the signal coming from each segment is low. Therefore it is necessary to perform an intermediate iteration which allows to start the last iteration with an higher signal. This would however cost additional time.

4.2 Creating a focus optimizing on the fluorescent signal

We propose a second method allowing to create a focus behind a turbid layer, based on the maximization of the fluorescent signal coming from a nanobead placed behind the layer [38].

The advantage of this method is that it allows to create a focus without having direct access to the sample. The quality of the focus is comparable to the previous method. The disadvantage is the longer time of execution. This would be a problem for applications with not fixed samples, as in vivo imaging.

4.2.1 Principle

To create the focus we optimize the phase of the different segments of the SLM in such a way that the integrated fluorescent intensity on the camera is maximized. Thus even in the absence of optical access, there is a contrast mechanism, which can be used to guide the wave-front optimization, since the maximization of the fluorescent intensity corresponds to an enhanced illumination of the fluorescent particle. In the presence of a single fluorescent particle, as was the case in [37], this directly means that we are creating a focus on that bead.

Similarly to the method presented in the previous section, the optimization algorithm works on segments, i.e. blocks of pixels, defined over the surface of the SLM. Each segment is processed by the optimization algorithm described above. Since the fluorescence signal is low compared to the background, we need to start with large segments to increase the signal. The algorithm can be reiterated with smaller segments until the desired intensity magnification is reached.

Notice that, this algorithm does not have a notion of the source of the fluorescence. More specifically, in the case of multiple fluorescent beads, the algorithm does not know about them. The optimization will only consider the overall intensity, and optimize for it. This means that there are several local minima, which can be arrived at by an optimization. Therefore in the presence of several fluorescent sources a single optimization will not necessarily give a focus on a single bead. However, when iterating the optimization, a process akin to that observed in acoustic waves can be followed. Given the different starting conditions, where some fluorescent sources are strongly illuminated, the optimization will lead to a stronger illumination of the already selected sources leading to a successive enhancement of the strongest source. This process is strongly enhanced by a non-linear response of the fluorescent particles to the illumination. We refer to this with the notion of 'selection'.

4.2.2 Image processing

Since the fluorescent signal is low compared to the noise of the camera, we apply image processing to isolate the nanobeads from the background, and define regions of interests around them. By looking in these areas, we are sure that we are optimizing the signal coming from the nanobeads and not some background noise.

The isolation of the nanobeads is obtained as follows:

First, we apply thresholding on the camera image. In our experiments the thresh-

old was set manually, but it can also be derived by computing the camera average and multiply it by a given factor. The thresholding separates the pixels into background and foreground sets. Most of the noise falls into the background set.

Since the response of the nanobeads may be weak, and hence close to the threshold value, pixels may be classified incorrectly, resulting in sparse noise across the image, and holes within the foreground blobs. As second step, we apply a combination of morphological opening and closing (Figure 4.4). Opening consists in an erosion followed by a dilation and allows to remove the remaining scattered noise. Closing consists in a dilation followed by an erosion and allows to fill possible small holes that have appeared on the beads while thresholding and opening.

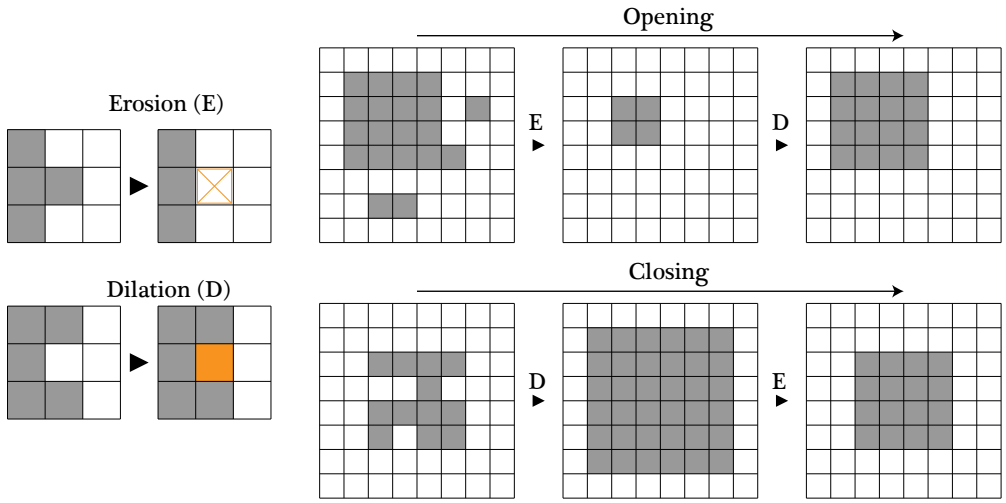

Figure 4.4 – Erosion assigns to a pixel the value 0 if most of the pixel around him have a value of 0. Dilation assigns to a pixel the value 1 if most of the pixel around him have a value of 1. Opening consists in an erosion followed by a dilation, while closing corresponds in a dilation followed by an erosion. As shown, the application of opening and closing allows to remove spurious noise and close gaps.

At this point, we obtain a mask where foreground pixels define the region of interests. When the optimization algorithm tries to find the best SLM configuration to maximize the camera response, such response is computed by looking into these regions only. This greatly improves the convergence of the optimization algorithm, which may otherwise be biased by strong background noise areas and try to enhance these instead of the beads.

Identifying the Nanobeads

We further extends this method adding another step if image processing, which allows to count the nanobeads and find their position and size on the screen. This may be convenient when looking for particular structures of known size, to discard regions were multiple nanobeads are closely grouped together and appear as a single large blob, or when nanobeads of different sizes are used, and the desire is to focus on one type only.
Given the filtered binary mask, we apply a procedure that guesses the number of nanobeads in the image, and applies k-mean clustering ([42]) to find the beads and assess if the guess was correct.

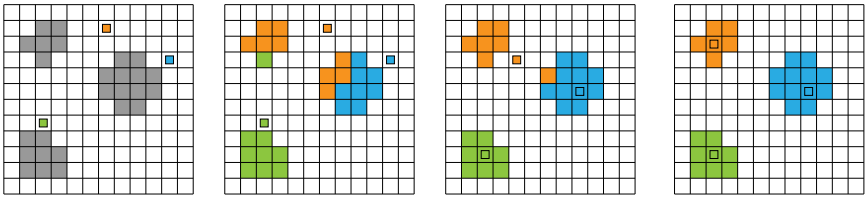

Figure 4.5 – This figure shows the application of the k-mean clustering algorithm to the binary input (a) with $k = 3$. In the first step, the three group centers are assigned randomly. Pixels are assigned to the groups based on proximity and the group centers are moved to their mean position (b). This process is repeated (c, d) until convergence, i.e. when the group of pixels do not change anymore.

First, let see how k-mean clustering works. A schematic representation is shown in Figure 4.5. This algorithm requires a given number k, which in our case is our guess for the number of nanobeads in the image. The algorithm starts by creating k empty sets, and associates each set to a random position in the image, which will be considered the center of the set. Then, for every foreground pixel, the distance to the closest set - using the center - is computed, and the pixel is added to the closest set. Once all foreground pixels have been assigned to one set, the center of the set is recalculated as the mean position of all pixel in the set. The procedure can now be repeated, i.e. the set are emptied, and pixels get assigned to them based on the new centers. In general, this algorithm converges pretty fast. In our experiment the centers would stop moving noticeably after three iterations.

The k-mean clustering algorithm requires to know the number k. We guess this value using the strategy depicted in Figure 4.6. We start assigning $k = 1$ and run k-mean clustering. As result, we get a set S of foreground pixels, and we

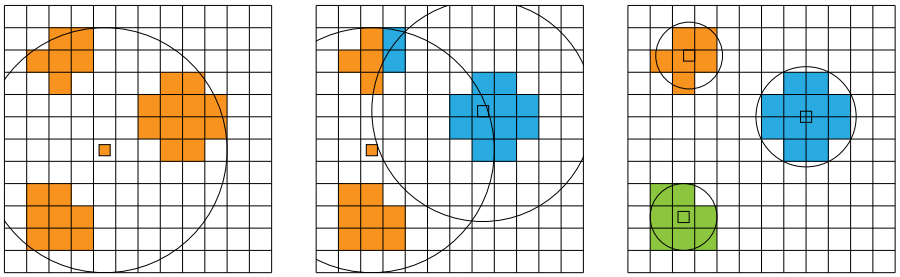

Figure 4.6 – This image shows the application of the k-mean clustering to the same input image with k values of 1, 2 and 3. Notice how in (a) and (b), the incorrect guess of k leads to large circles where only sparse regions are foreground pixels. Instead, the correct guess (c) leads to circles of appropriate radius, mostly containing foreground pixels.

can construct a circle c around the set mean, with radius r set to the distance from the mean to the pixel further away. Two criteria can be used to decide if the guess is appropriate. The simplest approach is to threshold based on the expected size of the nanobead. As shown in Figure 4.6.a), a large radius is likely the indication of the wrong estimation of k. A more robust alternative is to look at the ratio between foreground and background pixels within the circle c. If k is wrong, as in 4.6.b) and c), the circle may contain multiple nanobeads separated by empty space, resulting in a much low ratio. If k is correct, as in 4.6.c), the circle should mostly contain foreground pixels. If k appears to be wrong, we increase it by one, and repeat the procedure above, until we find the correct guess.

Once we are satisfied with our choice for k, we have a guess for the centers and radii of the nanobeads on the camera image.

4.2.3 Setup and samples

The sample consists in a 2mm thick glass-plate with a diffusing 1500 grit polished side 6 μm thick, corresponding to a few mean free paths. On the back, fluorescent nanobeads of 450 nm diameter are applied. The maximum of the excitation spectrum is at 480 nm, while the maximum of the emission is at 530 nm.

The setup is similar to the one used in the previous experiment. A schematic representation is shown in Figure 4.7. Since the fluorescent signal is anisotropic, the detector could in principle be positioned at each point around the sample.

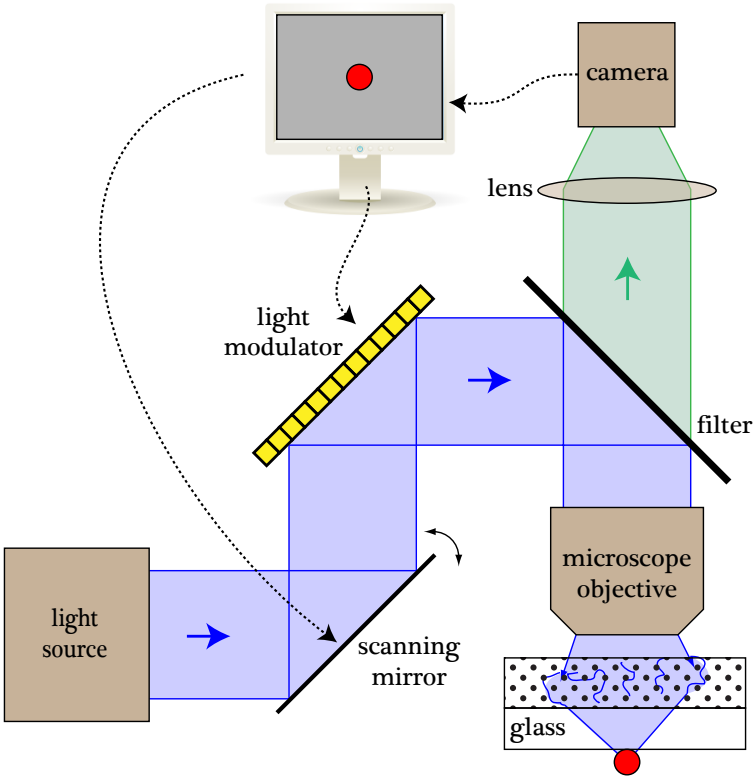

Figure 4.7 – Schematic setup of the experiment. The expanded laser beam goes through a galvoscanner which allows to move the focus on a x-y plane. It then goes on the SLM, and is imaged on the surface of the sample. The fluorescent light is collected by a camera located behind a fluorescence filter. The sample is a 2mm thick glass, with a diffusing 1500 grit polished side. On the back of the glass, there are fluorescent latex beads of 450 nm diameter.

4.2.4 Experimental results

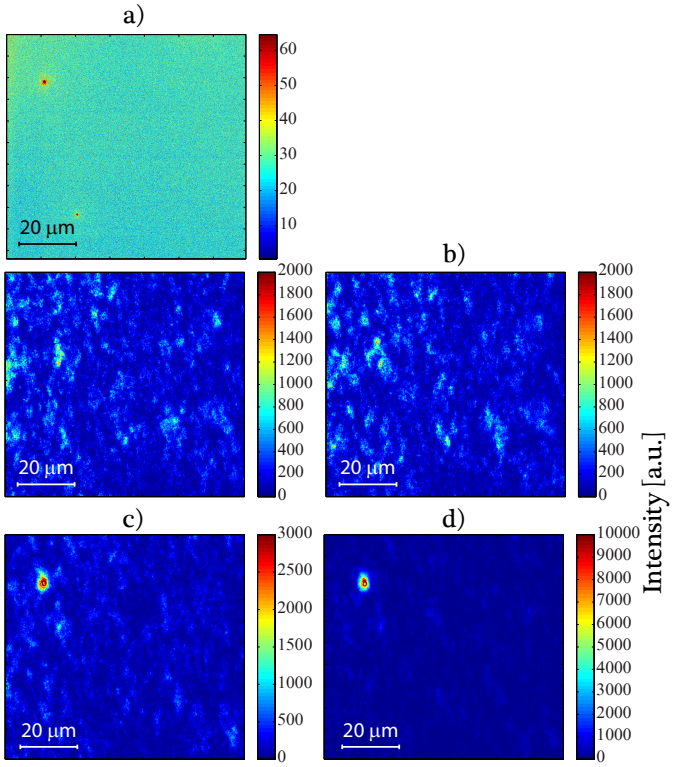

Figure 4.8 – Panels a) show a direct image of the fluorescent structures behind the turbid layer, consisting of two 450nm big fluorescent beads, and the transmitted light at the initial state. Panels b) through d) show the transmitted light distribution after successive iterations with 7x7 (b), 14x14 (c) and 28x28 (d) segments on the SLM. The intensity of the focus increases with the number of segments, while the fluorescence intensity decreases eventually due to photobleaching.

In Fig. 4.8 we show a focus created on a 450 nm diameter fluorescent bead behind a turbid layer after three iterations of the optimization algorithm, with different number of segments on the SLM: 7x7, 14x14 and 28x28. The fluorescence image of the initial situation shows two beads. The optimization process selects the most emitting one, i.e. it results in the most emitting one being focused on. As said above, the intensity of the focus depends on the number of segments on the SLM [7]. With 28x28 segments we obtain an amplification of the intensity of about 200 times. The first iterations are needed to increase the signal with respect to the background, otherwise the contribution of the small segments can not be detected.

The focus shows a pattern coming from diffraction effects, since the dimension of the bead is of the order of the wavelength.

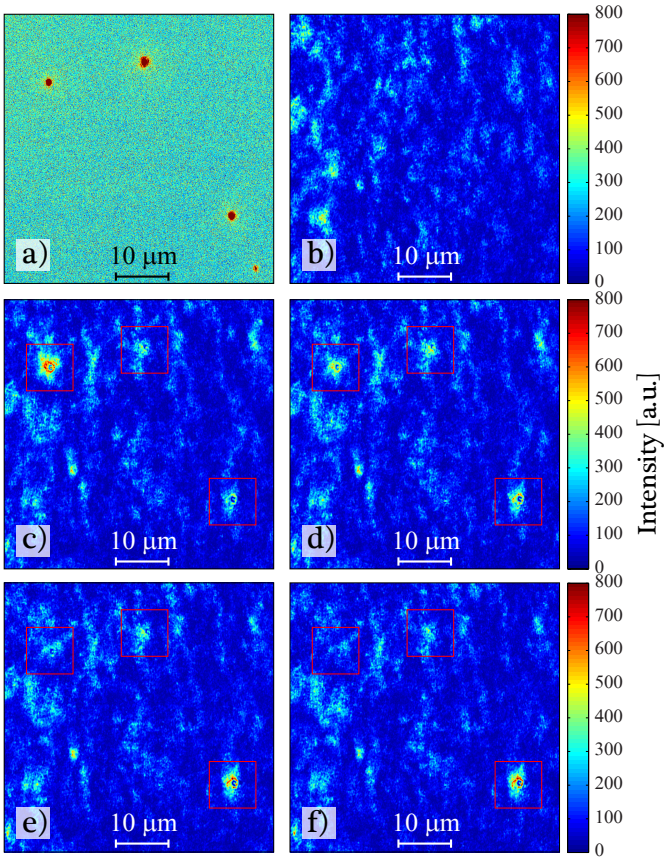

Figure 4.9 – The topleft panel (a) again shows the direct image of a set of four fluorescent particles (450 nm in diameter) hidden behind a turbid screen. Panel b) shows the transmitted light at the initial state. Panels c) through f) show the transmitted light after successive iterations with 14x14 segments controlled on the SLM. The red squares indicates the positions of the beads. After the fourth iteration with 14x14 segments the system selects one bead and a single focus is left.

If there are more beads emitting similar intensity on the sample the system can initially create several foci. As noted above, iteration of the optimization leads to a choice of a different local maximum, such that, after some iterations, a single focus is obtained. This is shown in Fig. 4.9, where the iteration procedure is shown for a situation where several particles of comparable intensity are in the field of view, but we are still left with a single focus after a round of four itera-

tions. In this case, the illumination time after an iteration was very long, such that the initially enhanced bead showed photo-bleaching in successive iterations. However in these iterations the next brightest bead is selected. Note also that in Fig. 4.9, the number of optimized segments is small, such that bright speckle spots are only weakly suppressed by the focus. A case with even more fluorescent sources is shown in Fig. 4.10. As can be seen in the sequence of iterations, the selection of a fluorescent bead depends on the brightness of the initial speckle illumination as well as the inherent brightness of the fluorescent beads. This shows that, even starting from complicated fluorescent structures, it is always possible to get a focus.

In the next chapter it will be shown that the quality of the focus is high enough to allow the imaging of a complex fluorescent structure.

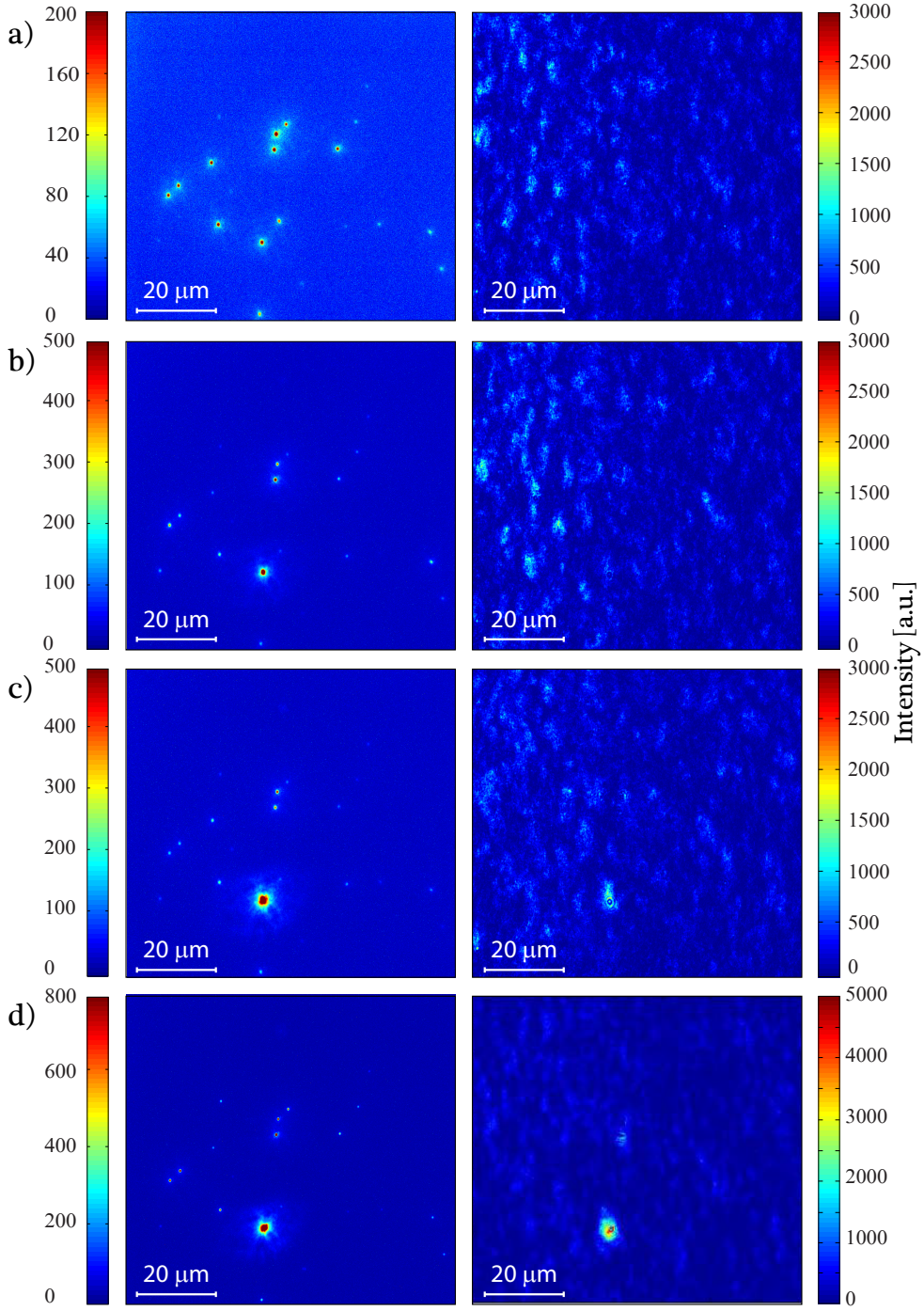

Figure 4.10 – In the presence of a large number of beads, the iterative scheme still works. a) show a field of view with more than 10 fluorescent sources ant the transmitted light. Panels b) to c) show the field of view (first column) and the transmitted light (second column) after iterations with 7x7 (b), 14x14 (c) and 28x28 (d) segments. At the end there is only a focus on a single fluorescent particle.

5 3D scanning

In this section we show how to move the focus in the $x - y$ plane, perpendicular to the beam direction, and respectively in the z direction.

While moving the focus on fluorescent samples, and measuring the emitted fluorescent at each position of the focus, it is possible to reconstruct an image of the sample.

We show the results of the scanning in the three dimensions and we briefly discuss the differences in resolution depending on the direction of scanning.

5.1 Scanning in the x-y plane

We scan the focus on a $x - y$ plane perpendicular to the beam. This method is based on the memory effect, explained in the theoretical section, and the instrument which allows us to move the focus around is a galvanometer scanner, a device consisting in two mirrors able to tilt the beam in two directions, as explained in the technical section.

This method allows to create a two-dimensional image of a fluorescent structure hidden behind a turbid medium.

5.1.1 Principle

Thanks to the optical memory effect, it is possible to move the focus on a $x - y$ plane behind a turbid layer simply by tilting the beam in the two directions, which corresponds to add a linear phase to the beam. For small angles, the phase configuration which leads to the focus is kept, even if the beam does not go exactly through the same paths. This allows to scan a small area by creating the focus only one time.

5.1.2 Setup and samples

For this experiment we used the same setup and the same samples as the ones we used for focusing without direct access, shown in section 4.2.3. We measure the fluorescent signal behind the sample but, since the fluorescence is emitted by the nanobeads anisotropically, it would be possible to measure it even at different positions. Measuring the signal behind the sample allows us to get a higher signal, since it does not go through the turbid layer.

5.1.3 Scanning range

In section 2.3.1 we have obtained equation 2.23 for the maximal scanning range in the x-y plane.

For our configuration we obtain a maximal angle of $\Delta\theta_{max} \simeq 5 \cdot 10^{-3}$ corresponding to a shift of $\Delta r \simeq 3.5\mu m$.

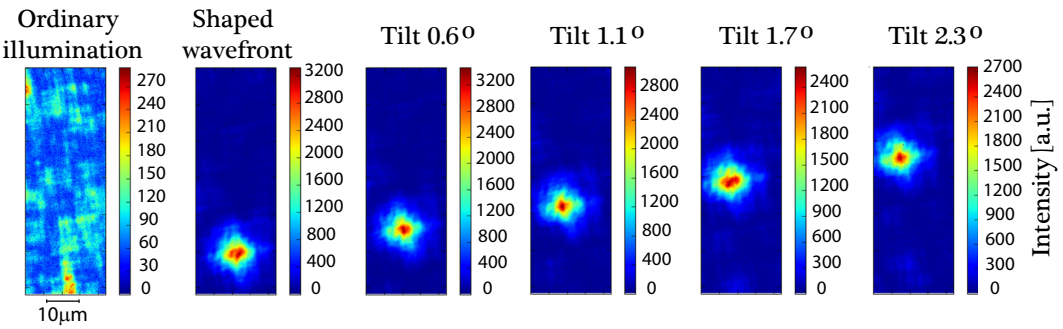

Figure 5.1 – This picture is from I. M. Vellekoop. The first panel shows the unshaped wavefront. The next panels show the focus at different angles.

Figure 5.1 shows images of the focus with different tilt angles. We observe that, as expected, the quality of the focus decreases with bigger angles.

Figure 5.2 is a plot of the intensity of the focus versus the scanning angle.

5.1.4 Experimental results

This experiment has been performed By I. M. Vellekoop.

Figure 5.3 shows the result of the scanning of a nanobead of 450 nm diameter in an area of 12x12 μm^2, with a focus created with the first method, meaning with direct access. Here the sample consists in a 1mm thick glass with zinc oxide on

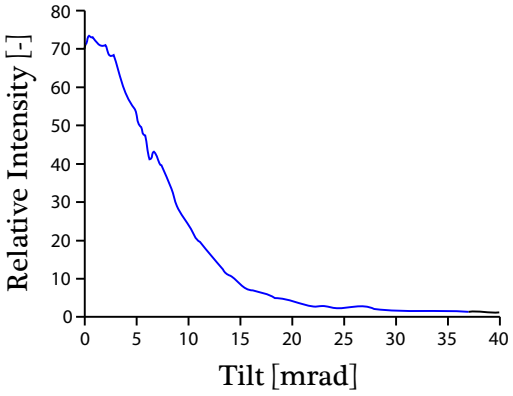

Figure 5.2 – This picture is from I. M. Vellekoop. It shows the relative intensity of the focus versus the scanning angle. The intensity of the focus is kept high enough until a tilting of an angle of about 5 mrad.

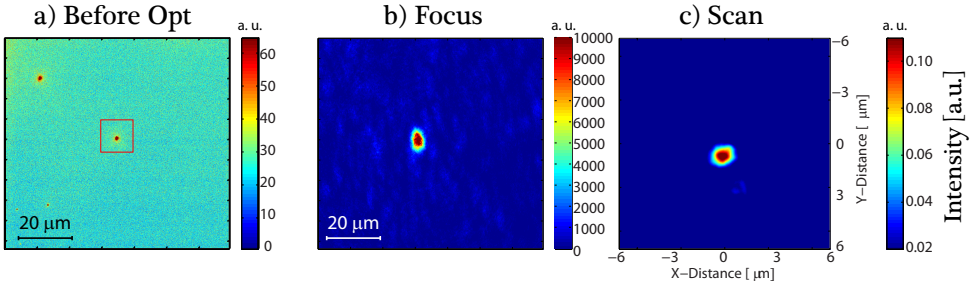

Figure 5.3 – a) shows the fluorescent beads on the sample, b) shows the focus obtained with 32x32 segments on the SLM with direct access and c) shows the result of the scanning. The red square shows the scanning area.

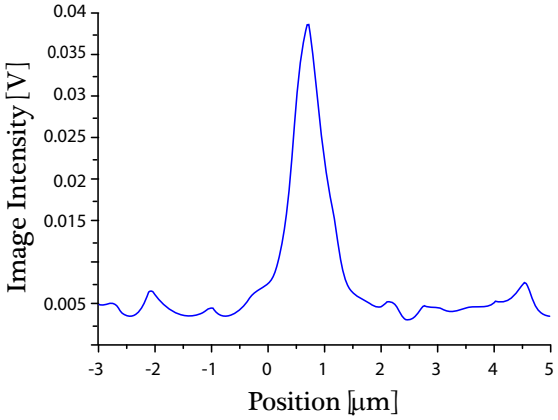

Figure 5.4 – The figure shows the intensity of a scanned fluorescent bead as a function of the position. The resolution in the x-y plane is 300 nm.

one side and the nanobeads on the back.

A plot of the intensity versus the position (Figure 5.4) gives a resolution of 300 nm Figure 5.5 shows the result of the scanning of a distribution of nanobeads of 450 nm diameter in an area of 24x24 μm^2, with a focus created with the second method, without direct access. The sample consist in a 2mm thick glass with one diffusive side and the nanobeads on the other.

In the measurement with the first method the focus was created with 32x32 segments on the SLM, while in the second measurement with 30x30 segments.

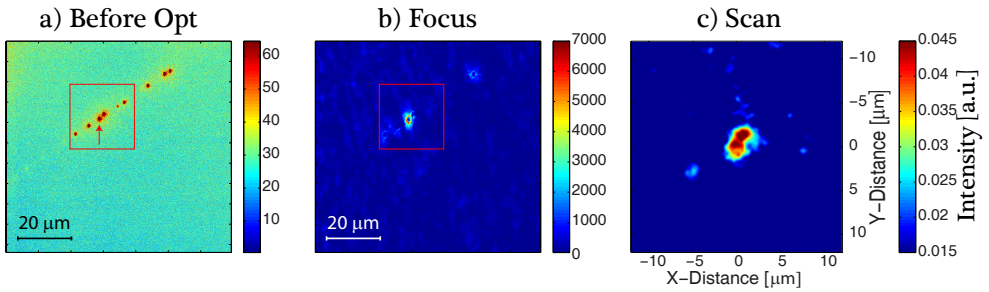

Figure 5.5 – a) shows the fluorescent beads on the sample, b) shows the focus obtained with 30x30 segments on the SLM without direct access and c) shows the result of the scanning. The red squares show the scanning area. The beads which are not in the center of the image are more difficult to detect because of two reasons: they have to be exactly on the x-y plane to be detected, and the intensity of the focus decreases the more it is far away from the center.

5.2 Scanning in the z direction

We add the third direction to the scanning through a variation of the optical memory effect. To move the focus along the z-axis we add a quadratic phase to the beam by means of the SLM.

5.2.1 Principle

As we have discussed previously, the memory effect leads to a retention of correlation of the phase over an angular scale determined by the thickness of the turbid medium.

To move the focus along the z axis, we need to add a curvature to the incoming light field. We do it by adding a parabolic shift to the SLM, where the radius of

curvature, R, corresponds to $1/R = \Delta z/a^2$, Where a is the distance between the turbid layer and the focal plane ($1mm$ in our case), and Δz is the shift of the focus in the z direction.

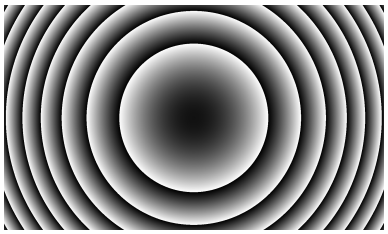

Figure 5.6 – An example of greyscale image added to the SLM after the optimization to shift the focus along the z axis.

We produce different greyscale images corresponding to the phase shift needed for each step of the scanning along the z axis, which will be added to the optimized phase on the SLM one after the other. Figure 5.6 shows an example of the phase shift: it can be seen that it corresponds to a spherical lens. Since the SLM has a maximum phase shift of 2π, the phase needs to be wrapped.

5.2.2 Setup and samples

To perform this experiment we used the same setup and the same samples as the ones used for the scanning in the $x - y$ plane.

5.2.3 Scanning range

In section 2.3.2 we have obtained equation 2.26 for the maximal scanning range in the z direction.

With our configuration we obtain $\Delta a_{max} = 60\mu m$.

The field of view obtained in the $z$direction can be increased with respect to that in the xy plane. This is true as long as the size of the illumination is smaller than the distance of the structure of interest from the scattering layer. However, this difference also leads to an anisotropy in the size of the focal spot.

In the z-direction, the focal spot will be larger by a factor of a/r as compared to the xy direction. This is because of the difference in path lengths in the different directions causing the interference based focus.

With the geometry described above, we expect a resolution in the xy plane given by half the wavelength of the light used, i.e. 250 nm and a resolution in the z-direction of 3 μm.

5.2.4 Experimental results

In Fig. 5.7, we show the fluorescence image of a $450nm$ diameter bead hidden behind a turbid layer. The in-plane image has a resolution of $300nm$, as it has been shown before [20], thus showing the size of the beads (see part (e)) of the figure, where the bead is fully in focus). The subsequent part of the figure show successive scan images of the same particle using a wave-front shaped focus, i.e. behind the turbid layer. The images are made at different nominal positions of the focal point, where the imaging plane is shifted in the z direction by $2\mu m$ in every step, except between part (d) and (e) as well as (e) and (f), where the step size is one micron. The scanning through the bead can be clearly seen and a cut through the z-direction at the bead position yields the resolution that is obtained in this way. As discussed above, the scan range of the image is limited by the correlation length implied by the memory effect. The size of the image in the plane reflects the maximum scanning range, where the intensity in the focus has decreased by a factor of 2. This implies that a fluorescent bead at the edge of the image would be less intense by roughly a factor of 2 than one in the center. In the z-direction, the scan range shown in Figure 5.5 is much smaller than the theoretical limit, such that effectively the intensity in the focus is constant for all images.

The resolution in the $z-$direction is presumably somewhat lower than in the xy plane, as can be seen from the bigger scanning range discussed above and the corresponding smaller adjustment in the phase shift for the same shift of the focus. This is shown in Figure 5.8, where we show the fluorescent intensity at the position of the bead as a function of scanning depth. The resolution turns out to be $3.0(1)\mu m$ as measured by the half width at half maximum. This reduction in resolution however goes together with an increase in scanning range in the z-direction as discussed above.

In order to test the scanning range implied by the theoretical consideration above, we have also carried out an experiment with two fluorescent beads that have been hidden behind the same turbid screen, but where the second particle was shifted in the z-direction by a spacer of $55\mu m$. This corresponds to the scan range implied by the memory effect for our geometry, such that an image should still be possible at this distance however with worse quality. The change in phase incurred over that distance leads to a deterioration of the focus by roughly a factor of two with a corresponding change in resolution. The results of this are shown

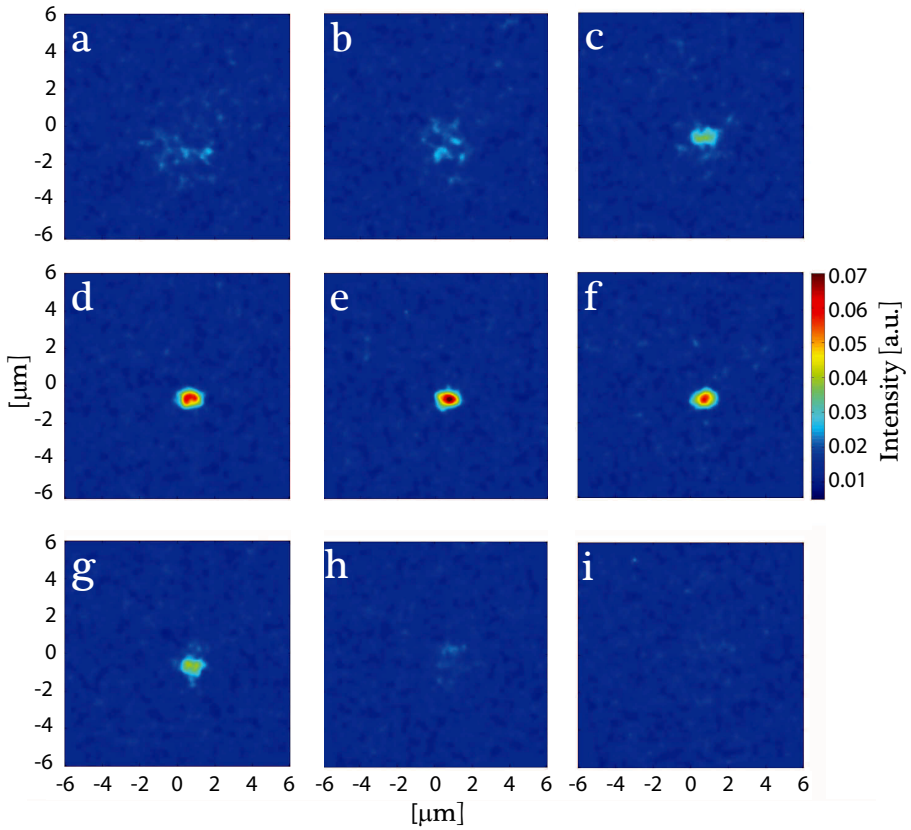

Figure 5.7 – (a)-(i) The fluorescence signal of a 450 nm diameter fluorescent bead hidden behind a turbid layer. The images show the scattered light fluorescence image of the same bead and on the same intensity scale, while the position of the focal plane differs for the images. In (a), the position is at -7 μm behind the bead and consecutively moves forward in steps of 2μm, until it lies 7 μm in front of the bead position in image (i). The center of the bead, which would therefore lie between image (d) and its neighbor has been added as well in part (e). Thus, the difference in z position between parts (d) and (e) as well as (e) and (f) corresponds to only 1 micron. The scan range in this case is a window in the x-y plane of 12x12 μm^2. The three dimensional structure of the bead can be clearly seen.

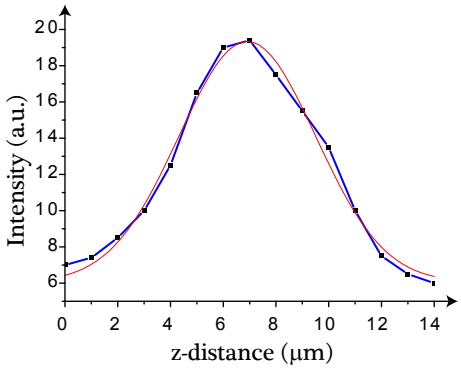

Figure 5.8 – The point spread function of the scattered light fluorescence microscope in the z-direction. The figure shows the intensity at the position of a fluorescent bead as a function of scanning depth. In contrast to 5.5, we show the full scanning range with a step size in the $z-$direction of $1\mu m$, giving a better measure of the depth resolution. This shows that the resolution in the $z-$direction is about $3\mu m$ half width at half maximum, which is somewhat worse than in the xy plane thus showing that the interference focus is asymmetric. The red line shows a Gaussian fit with a standard deviation of $2.6(1)\mu m$.

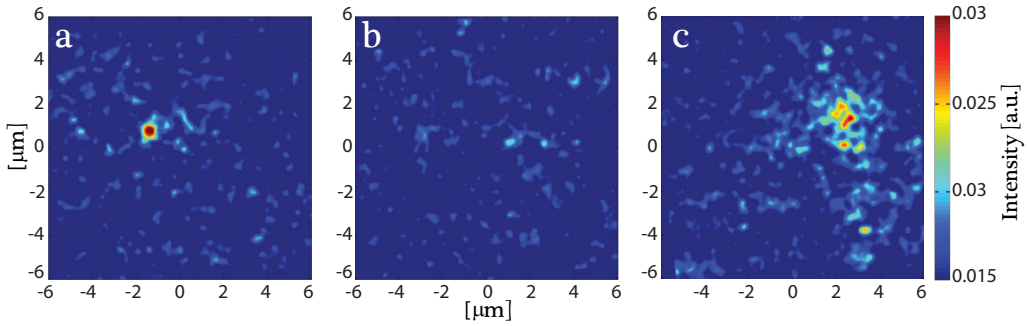

Figure 5.9 – (a)-(c) The fluorescence signal of two 450 nm diameter fluorescent beads hidden behind a turbid layer. The two beads are 55 μm apart in the z-direction and are at positions (-2,-1) and (2,-2) respectively in the $x-y$ plane. The images show the scattered light fluorescence image on the same intensity scale, at three different depth. In (a), the position is at the first bead, whereas at (b) the position is 30 μm towards the second particle. Figure (c) finally is at a z position of 55 μm corresponding to the position of the second particle. The scan range in this case is a window in the $x-y$ plane of 12x12 μm^2. As discussed in the text, the z scan-range is 60 μm explaining the deteriorating quality of the image of the second particle. However, the three dimensional structure of the beads' positioning can be clearly seen.

in Figure 5.9, where the first particle (in the plane of the initial focus) is shown in part (a), an intermediate $x-y$-scan is shown for $z = 30\mu m$ in part (b) and finally the second particle is shown in part (c) at a position of $z = 55\mu m$. While clearly a particle can be seen in Figure 5.9 (c), the resolution is worse than that shown in Figure 5.9 (a) because of the limitations in scan range implied by the memory effect. The distance in the z direction covered by the scanning corresponds well to that of the theoretical expectation.

With the scanning along the z axis, combined with the one in the $x - y$ plane, it is now possible to move the interference based focus, obtained by wave-front shaping, in all three directions of space. The field of view obtained with this technique determined by the memory effect is of sufficient size to be of interest in biological applications.

6 Improving the quality of the image

In this chapter we present an attempt to improve the quality of the image. Basically with quality of the image we mean how good one can identify the different elements of the image.

We must however express this statement more precisely. In classical optics one relates the quality of optical instruments (like a telescope or microscope) to the concept of angular or spatial resolution, which is the ability to distinguish points that are located at a small angular distance. The resolution power is limited by diffraction. It is then straight forward to connect a gain of resolution to an increase of information.

The concept of resolution is harder to handle in the domain of image processing. We therefore limit our efforts to try to get an improvement of the image through a contours enhancement. An image with enhanced contours is sharper. We will see, that it can happen that, through contour enhancement, two points of an image that could not be separated in the original image, can be distinguished. Nevertheless we cannot speak of an increase of information. In section 6.2.2 we will show this through a computation, but it can be also seen intuitively. Even if it is easier to distinguish to near objects in an enhanced image with respect to the original, the enhanced image will not show objects between the two considered objects which were not present in the original image.

Inspired by filtering techniques used in classical image processing, we will try to enhance the contours of the result of the scanning by subtracting to it an image got by a scanning with a ring.

Our procedure is thus the following:

1. We first look at which phases distribution do we need on the SLM to transform a focus into a ring.

2. We create a focus through the optimization process and perform a scanning.

3. We modify the focus into a ring by adding to the result of the optimization what we have found in 1., then we scan the object with the ring.

4. We subtract the image obtained at point 3. from the one obtained in 2. in order to get the contour enhanced image.

6.1 Adding a pattern to the focus

The first step in the process of the contours enhancement consists in being able to transform the focus in a desired pattern, a ring in this case.

We do this by adding a local phase delay on the SLM, after the optimization process.

6.1.1 Transforming the focus into a ring

In this section we compute the phase distribution that we need to add to the phases computed with the optimization algorithm, so that the focus is transformed into a ring.

Transforming the focus into a ring corresponds to create a minimum of the intensity of the light at the position of the focus, and a maximum around it. Creating a minimum of intensity means create destructive interference, in such a way that light contributions coming from the different portions of the beam cross section annihilate each other at the position of the focus.

Figure 6.1 – A circular gradient going from a greyscale value of 0 to a greyscale value of 255, corresponding to a phase shift of 2π. This is the image we load on the SLM after the optimization process to obtain the ring-shaped focus.

There are obviously unlimited ways to create destructive interference. We choose a distribution of the phase delays as shown in Figure 6.1. It is a circular gradient going from a phase delay of 0 to 2π, centered in the middle of the cross section of

the beam. Opposite radius are out of phase of π, meaning they interfere destructively. This pattern is not too sensitive to a non uniform intensity distribution.

The intensity profile resulting from the add of a phase delay following a circular gradient can be computed as follows: we define as $E_0(x, y)$ the field at $z = 0$, on the SLM plane, the field on the focal plane ($z = f$) is given by

$$E_1(\xi, \eta) = \iint dx \cdot dy \cdot E_0(x, y) \cdot Q(\phi) \cdot e^{-i \cdot k \cdot \frac{\xi \cdot x + \eta \cdot y}{f}} \tag{6.1}$$

where

$$Q(\phi) = e^{i \cdot \phi} \tag{6.2}$$

is the phase delay, x and y are the two components of the position vector $\vec{r}$ in the SLM plane, ϕ is his angle, and ξ and η are the two components of the position vector $\vec{s}$ in the focal plane wit his angle β, and $\xi \cdot x + \eta \cdot y$ their scalar product.

We change the coordinate system in polar coordinates. The scalar product can be written as

$$\vec{r} \cdot \vec{s} = r \cdot s \cdot \cos(\phi - \beta). \tag{6.3}$$

For the field we obtain

$$E_1(s, \beta) = \int_0^R dr \cdot r \oint d\phi \cdot e^{i \cdot \phi} \cdot e^{-i \cdot k \cdot \frac{r \cdot s \cdot \cos(\phi - \beta)}{f}} \tag{6.4}$$

where R is the radius of the laser beam.

We define the angle $\theta = \phi - \beta$. The field becomes

$$\begin{aligned} E_1(s, \beta) &= \int_0^R dr \cdot r \oint d\theta \cdot e^{i \cdot \theta} \cdot e^{i \cdot \beta} \cdot e^{-i \cdot k \cdot \frac{r \cdot s \cdot \cos\theta}{f}} \\ &= e^{i \cdot \beta} \cdot \int_0^R dr \cdot r \oint d\theta \cdot e^{i \cdot \theta} \cdot e^{-i \cdot k \cdot \frac{r \cdot s \cdot \cos\theta}{f}} \\ &= e^{i \cdot \beta} \cdot \int_0^R dr \cdot r \cdot J_1\left(k \cdot \frac{r \cdot s}{f}\right) \end{aligned} \tag{6.5}$$

where $J_1\left(k \cdot \frac{r \cdot s}{f}\right)$ is a Bessel function of the first order.

We notice that, in the same way, the field of the focus is given by

$$E_0(s,\beta) = e^{i\cdot\beta}\cdot\int_0^R dr\cdot r\cdot J_0\left(k\cdot\frac{r\cdot s}{f}\right). \tag{6.6}$$

We can rewrite the formula in a general way

$$E_n(s,\beta) = e^{i\cdot\beta}\cdot\int_0^R dr\cdot r\cdot J_n\left(k\cdot\frac{r\cdot s}{f}\right) = e^{i\cdot\beta}\cdot F_n(s) \tag{6.7}$$

where for $n = 0$ we have the focus while for $n = 1$ we have the ring.

Figure 6.2 shows the two intensity profiles.

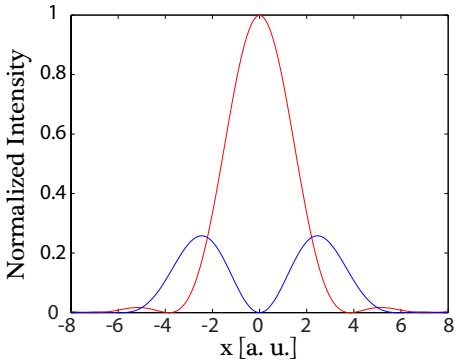

Figure 6.2 – The red curve represents the intensity profile of the focus, the blue curve represents the intensity profile of the ring, obtained by adding a "circular-gradient-phase" to the focus.

6.1.2 Experimental results

We have tried to transform the focus into a ring using the same setup we used for the focusing with direct access. The samples were the same as we used for the focusing without direct access.

Figure 6.3 shows the light distribution after the optimization (a), the light distribution after applying the circular gradient on the SLM (b) and their profiles of the focus (red) and the ring (blue) in the x (c) and y (d) directions.

6.2 Experimental contours enhancement

In this section we describe an attempt to use the scanning with the ring to improve the quality of the image, meaning to increase the contrast of the contours.

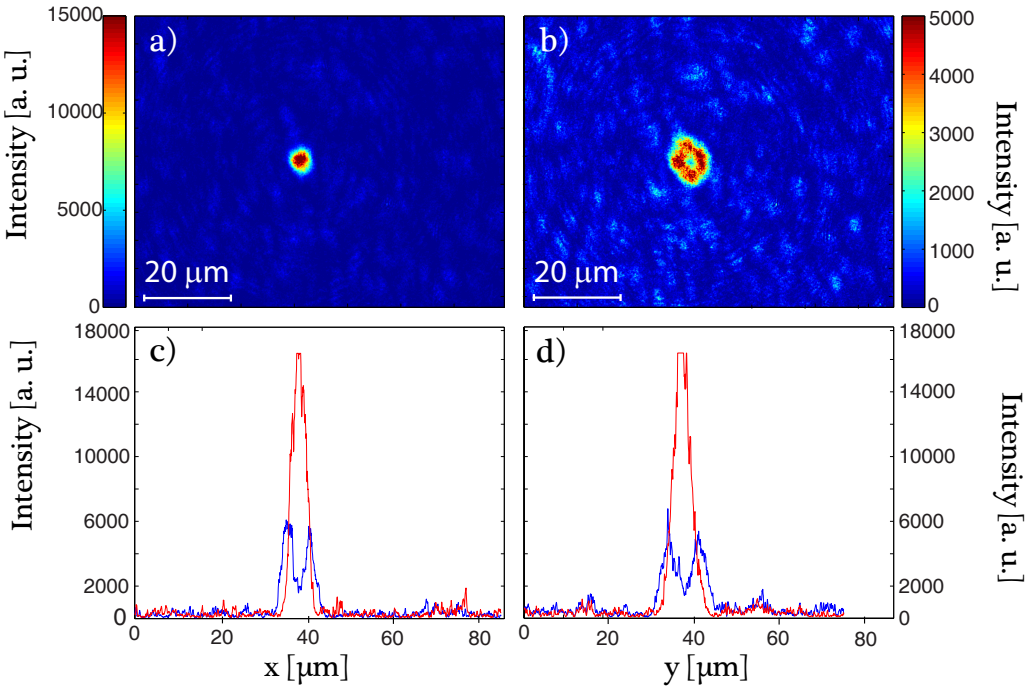

Figure 6.3 – Panel a) shows the focus, panel b) shows the ring-shaped focus, while panels c) and d) show they x and y profiles. The red curves correspond to the focus, while the blue curves to the ring.

6.2.1 Principle

The first step consists in scanning with the focus as explained in the previous chapter. The result of the scanning with the focus corresponds to a convolution between the focus and the real image. This means the smaller the focus is, the more the result of the scanning is near to the real image. The dimension of the focus is diffraction limited and this gives a limit to the maximal resolution of the scanning.

The second step consist in scanning a second time the same region, but with the ring instead of the focus. The result corresponds to a convolution between the real image and the ring.

Once the two measurements are done, we proceed with the subtraction of the second scanning to the first. In the next section we show that - as expected - this leads to an image where the contours are more sharp and where two near points are better distinguishable.

6.2.2 Theory and simulations

In this section we study the effect of the subtraction of the result obtained by scanning with the ring to the one obtained by scanning with the focus.

The scanned image Q_n corresponds to the convolution between the object B and the focal intensity distribution of the scanning beam and is given by

$$Q_n = I_n * B = \int_{-\infty}^{\infty} dx' I_n(x - x') \cdot B(x') \tag{6.8}$$

where I_n is the intensity profile of the focus (n = 0), respectively of the ring (n = 1) and B is the intensity of the object, which in our experiments would be the glass surface with the fluorescent nanobeads. The intensity of the result image is

$$Q_{01} = Q_0 - a \cdot Q_1 = (I_0 - a \cdot I_1) * B = I_{01} * B \tag{6.9}$$

where a is a mixing factor between 0 and 1. For the next computations we chose $a = 0.5$.

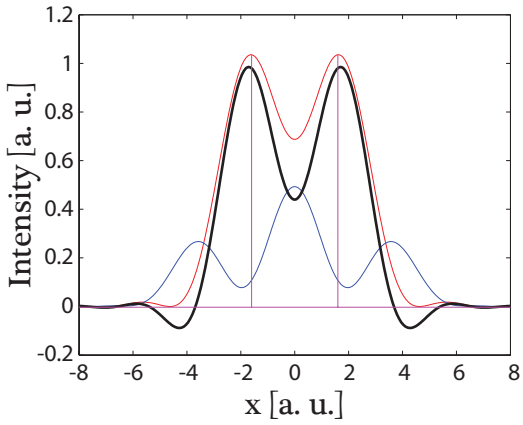

Figure 6.4 – The panel shows a Matlab simulation of scanning of two delta peaks with the focus, with the ring and the combination of the two scans. The pink curve corresponds to the object B, the red curve to the scan with the focus Q_0, the blue curve to the scan with the ring Q_1 and the dark curve to the result Q_{01}.

Figure 6.4 shows two Matlab simulations of the profiles Q_0, Q_1 and Q_{01} for an object B corresponding to two near points, i. e. two peaks. The pink curves corresponds to B, the red curve to Q_0, the blue curves to Q_1 and the dark curves

to Q_{01}. Q_{01} helps to distinguish the two points.

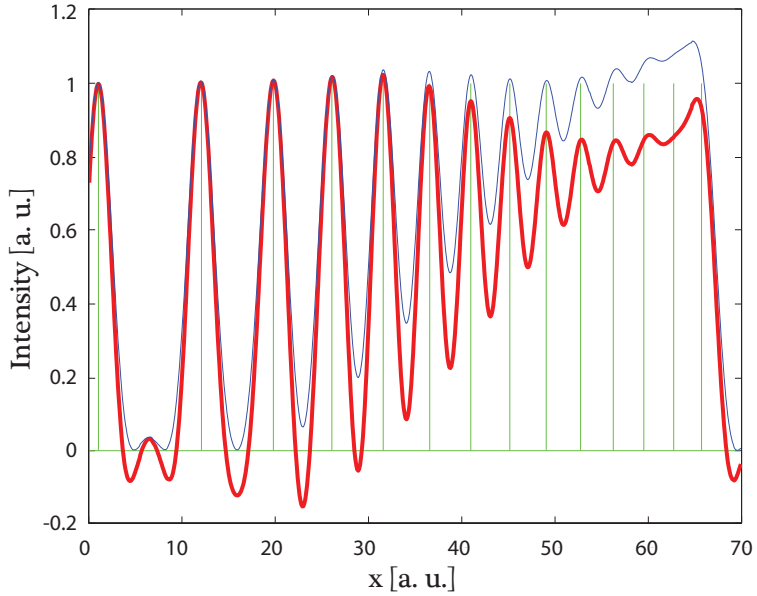

Figure 6.5 – A distribution of peaks (green) is scanned with the focus (blue) and then with the ring (red). The scanning with the ring is subtracted to the one with the focus and gives the red curve.

Figure 6.5 shows a simulation of the scanning with the focus (blue curve) and the result of the subtraction of the scanning with the ring to the one with the focus (red curve), for an object consisting in a distribution of always closer peaks (green). It can be observed that the scanning with the ring helps to accentuate the higher frequencies.

To deeply investigate the effect of the scanning with the ring, we look at the difference between the Modulation Transfer Functions (MTF) for Q_0 and Q_{01}. The MTF $g_n(k)$ says with which factor of amplification a harmonic function with wavenumber k is transmitted, meaning which frequencies from the real image B are transmitted through Q_0, respectively Q_{01}. It is defined by

$$Q_n = g_n(k)e^{i \cdot k \cdot x}. \tag{6.10}$$

This means that we assume:

$$B = e^{i \cdot k \cdot x}. \tag{6.11}$$

From equation 6.8 follows

$$
\begin{aligned}
Q_n &= \int_{-\infty}^{\infty} dx' \cdot I_n(x - x') \cdot e^{i \cdot k \cdot x'} \\
&= e^{i \cdot k \cdot x} \cdot \int_{-\infty}^{\infty} dx' \cdot I_n(x - x') \cdot e^{i \cdot k \cdot (x' - x)} \\
&= e^{i \cdot k \cdot x} \cdot \int_{-\infty}^{\infty} du \cdot I_n(u) \cdot e^{i \cdot k \cdot (u)} \\
&= e^{i \cdot k \cdot x} \cdot \tilde{I_n}(k) \qquad (6.12)
\end{aligned}
$$

where $\tilde{I_n}(k)$ is the Fourier transform of the intensity.

This gives

$$g_n(k) = \tilde{I_n}(k). \qquad (6.13)$$

We now need to determine the Fourier transform of the intensity. We handle the problem in two dimensions.

Frmula 6.7 gives the field of the focus and of the ring. It follows for the intensity

$$I_n(s) \simeq F_n^2(s). \qquad (6.14)$$

The Fourier transform of the intensity is given by

$$
\begin{aligned}
\tilde{I_n}(s) &= \iint d\xi \cdot d\eta \cdot e^{-i \cdot (q_1 \cdot \xi + q_2 \cdot \eta) \cdot I_n(\xi, \eta)} \\
&= \int_0^{\infty} ds \cdot s \cdot J_0(q \cdot s) \cdot F_n^2(s) \\
&= \int_0^{\infty} ds \cdot s \cdot J_0(q \cdot s) \cdot \left(\int_0^{R} dr \cdot r \cdot J_n(k \cdot \frac{r \cdot s}{f} \right)^2 . \qquad (6.15)
\end{aligned}
$$

We define two new dimension free variables

$$w = \frac{r}{R} \quad , \quad s_0 = \frac{f}{k \cdot R}. \qquad (6.16)$$

It follows

$$\tilde{I_n}(s) = \int_0^{\infty} ds \cdot s \cdot J_0(q \cdot s) \cdot \left(\int_0^{1} dw \cdot w \cdot J_n \left(w \cdot \frac{s}{s_0} \right) \right)^2 . \qquad (6.17)$$

With $u = \frac{s}{s_0}$ we have

$$\tilde{I}_n(u) = \int_0^\infty du \cdot u \cdot J_0(q \cdot u \cdot s_0) \cdot \left(\int_0^1 dw \cdot w \cdot J_n(w \cdot u) \right)^2 . \tag{6.18}$$

And finally, with $p = q \cdot s_0$ we get for the Fourier transform of the intensity

$$\begin{aligned} \tilde{I}_n(p) &= \int_0^\infty du \cdot u \cdot J_0(u \cdot p) \cdot \left(\int_0^1 dw \cdot w \cdot J_n(w \cdot u) \right)^2 \\ &= \int_0^\infty du \cdot u \cdot J_0(u \cdot p) \cdot I_n(u) \end{aligned} \tag{6.19}$$

which, as shown above (formula 6.13), corresponds to the MTF for a scanning with the focus $Q_0(n = 0)$ and a scanning with the ring $Q_1(n = 1)$.

The MTF for Q_{01} is given by

$$g_{01}(k) = \tilde{I}_{01}(k). \tag{6.20}$$

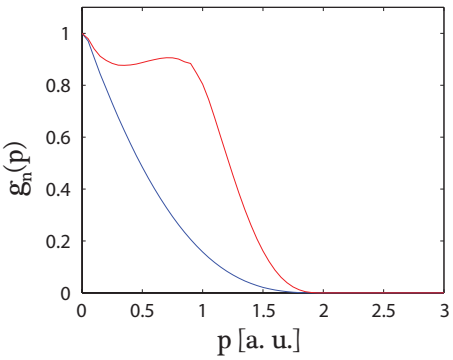

Figure 6.6 – The blue curve represents the MTF for Q_0, while the red curve represents the MTF for Q_{01}. On the abscissa: p is proportional to the wavenumber k.

Figure 6.6 shows the MTF for Q_0 and Q_{01} computed with Matlab. It can be observed that the two curves go to 0 at the same value of p (which is proportional to k), but $g_{01}(k)$ is higher than $g_0(k)$ for high frequencies. This means that Q_{01} accentuates better the high frequencies, but does not give additional information if compared to Q_0. This is actually the effect of a sharpen filter.

6.2.3 Setup and samples

The setup and the samples used for this experiment as the same as the ones used to focus without direct access, except that for a second kind of nanobeads: we performed part of the measurements with 200 nm beads, emitting in the green at 508 nm.

6.2.4 Experimental results

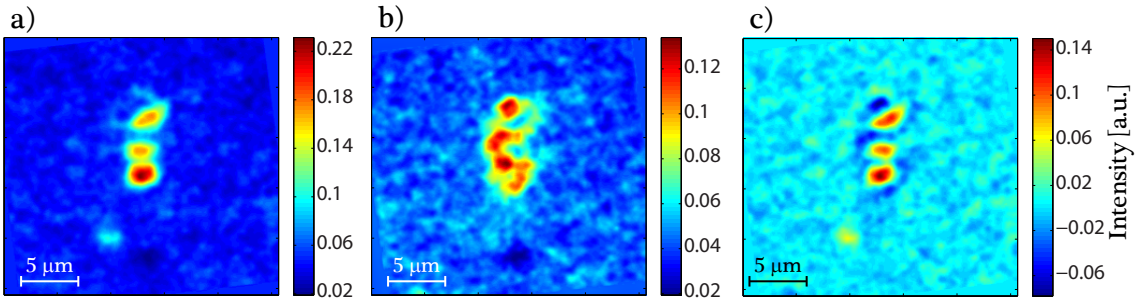

Figure 6.7 – Panel a) shows the scanning of a 200 nm nanobead with the focus, panel b) shows the scanning with the ring and panel c) shows the result.

Figure 6.7 shows the scanning with the focus, the scanning with the ring and the result of the subtraction of the second to the first.

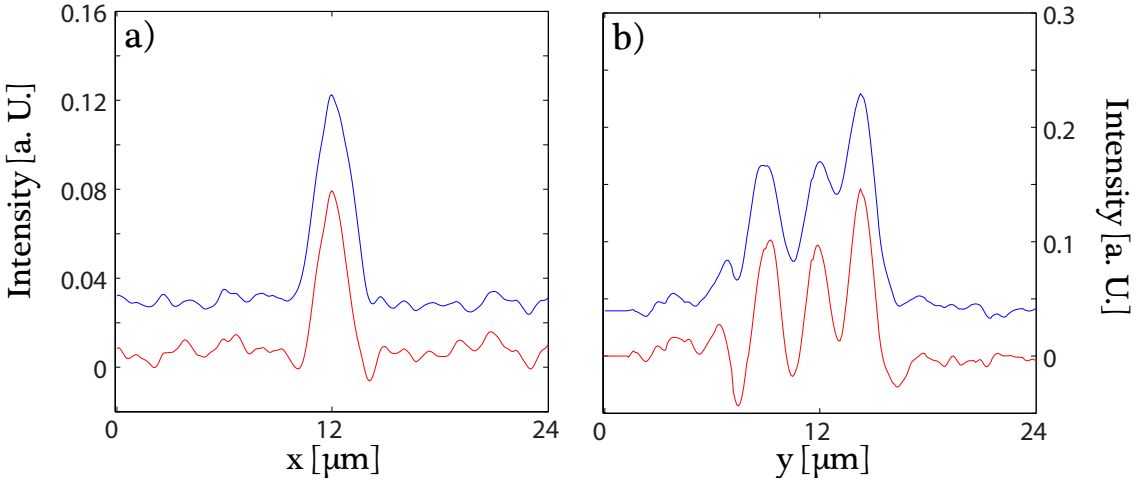

Figure 6.8 – Panel a) shows the intensity profiles of the scanning with the focus (blue) and of the result (red) in x, while panel b) in y.

Figure 6.8 shows the corresponding intensity profiles of two slices in the x and y directions.

The result does not show the expected quality. Along the y axis the profiles of the beads result more sharp, as expected from the Matlab simulation, but the same can not be said for the x direction. The measurement was very sensitive to the alignment of the setup. This is probably the reason of the difference of the quality in the two directions.

6.3 Contour enhancement through computation

In the previous section we discussed the possibility of contour enhancement by supplementing the scan Q_0 by the scan Q_1 with the ring shaped focus, and combining them. Interestingly enough, Q_1 can be calculated numerically from Q_0, which means, that the measurement of Q_1 is not necessary, at least in principle. In fact, from the Fourier transform of equation 6.8

$$\tilde{Q}_n = \tilde{I}_n \cdot \tilde{B} \tag{6.21}$$

we get

$$\tilde{Q}_1 = \frac{\tilde{I}_1}{\tilde{I}_0} \cdot \tilde{Q}_0 \tag{6.22}$$

which means, that we can compute the Fourier transform of Q_1 from the Fourier transform of Q_0 .

The factor

$$q_{10} = \frac{\tilde{I}_1(p)}{\tilde{I}_0(p)} \tag{6.23}$$

does not depend on the object B and can be calculated once and for all from equation 6.19. The dependence of q_{10} on p is displayed in Figure 6.9 Note that both, $\tilde{I}_1$ and $\tilde{I}_0$ vanish exactly (in the Fraunhofer approximation, images in the focal plane behind a finite aperture are band-limited) for $p > 2$, and a necessary condition for this recipe to work, $\tilde{I}_0 \neq 0$ for $0 < p < 2$, is satisfied.

For noisy objects, contour enhancement by actually measuring Q_1 may provide information on the object superior to results of the numerical method sketched here. However, this issue, which would be of great interest, is beyond the scope of the present work.

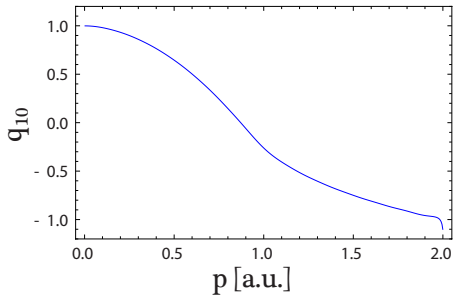

Figure 6.9 – The factor q_{10} used to calculate Q_1 from Q_0.

6.4 Conclusive considerations and outlook

We have shown that the scanning with a ring allows to enhance the contours - and therefore an improvement - of the image obtained through the scanning with the focus. This improvement allows to distinguish two objects which were not distinguishable on the original image.

If we define as resolution the capability of distinguish to near points, we can say that the scanning with the ring increases the resolution.

We have also shown that, for an ideal case, the same result can be obtained through a computation.

It is however not to exclude that, for non ideal cases, meaning in presence of noise, the experimental contours enhancement could have advantages with respect to the computation, which in those situations would be more complex. This problem is not trivial and could be the subject for a future research.

7 Conclusions

In conclusion, we have developed the main elements needed for fluorescence based microscopy, allowing imaging in three dimensions behind turbid layers.

We have proposed two methods with which to focus on fluorescent structures inside turbid media at diffraction limited resolution. The first one was a simple but invasive method, the second one was non-invasive. The bases of these techniques are iterative wave-front shaping on the transmitted light, and respectively the transmitted fluorescence. The first method allows focusing on a desired point, while the second one selects a single particle creating a scannable focus.

The scanning is possible due to the optical memory effect, which allows to keep the phase configuration of the focus while the focus is moved on a small area of the sample, and can be extended to three dimensions by the addition of a parabolic phase field to the SLM.

The resolution of the images is limited by the size of the interference based focus, which in turn is limited by the wavelength of the light used. However, it is neither determined by the optical elements used in the setup nor the scattering properties of the layer in front of the structure of interest.

The field of view available to the microscope is dependent on the distance to the turbid layer, as well as the thickness of the layer. It has previously been shown that in an egg geometry, similar to our artificial samples, a plane of 12x12 μm^2 can be imaged [20]. In the z-direction, we have shown that similar fields of view can be achieved. In fact, due to the way in which the distance between the layer and the structure of interest enters in the memory effect, the theoretically achievable field of view in the z-direction is actually bigger, in our case up to 60 μm.

Therefore, even structures close to the scattering layer could be studied in this way. With this possibility of three dimensional scanning of the focus, applications of scattered light fluorescence microscopy become possible.

We have proposed an experimental attempt to increase the quality of the image

through a second scanning performed with a ring-shaped focus. This system enhances the contours and helps to better distinguish near points but does not add information to the image. It would be interesting to show, in a future project, if this system works better than an image-processing filter for non ideal cases, i. e. in presence of noise.

The main drawback of the techniques remains in the temporal resolution, which is driven by the rate of change possible in the SLM used for the optimization. Currently this leads to long exposure times of several minutes per iteration for the focusing without direct access and of the order of 30 minutes for creating three dimensional images, such that applications can for the moment only be envisaged in static turbid media, i.e. where the turbid layer is stable on timescales longer than the focusing and scanning time. However, recent progress in the development of piezo-element based SLMs [45] make it possible to increase the speed of the SLM by at least three orders of magnitude [25], which makes applications possible. This can be seen by the time scale of the dynamics of fluctuations in e.g. Drosophila pupae, which is of the order of a minute [46]. Alternatively, phase conjugation may also allow an increase in temporal resolution [47].

Bibliography

[1] M. von Laue, *Mathematische Betrachtungen über die Beugungserscheinungen an vielen unregelmässig verstreuten Teilchen*, Mitt. Phys. Ges. Zürich, 18: 90-102 (1916).

[2] J.B. Pawley (ed.) *Handbook of Biological Confocal Microscopy (3rd ed.)*, Springer, Berlin (2006).

[3] F. Helmchen and W. Denk, *Deep tissue two-photon microscopy*, Nat. Methods **2**, 932-940 (2005).

[4] A. Diaspro, ed., *Confocal and Two-Photon Microscopy: Foundations, Applications and Advances*, Wiley-Liss, New York, (2002).

[5] C. Vinegoni, C. Pitsouli, D. Razansky, N. Perrimon, and V. Ntziachristos, *In vivo imaging of Drosophila melanogaster pupae with mesoscopic fluorescence tomography* Nat. Methods **5**, 45-47 (2008).

[6] M. Wolf, M. Ferrari, and V. Quaresima, *Progress of near-infrared spectroscopy and topography for brain and muscle clinical applications*, J. Biomed. Opt. **12**, 062104 (2007).

[7] I. M. Vellekoop and A. P. Mosk, *Focusing coherent light through opaque strongly scattering media*, Opt. Lett. **32**, 2309-2311 (2007).

[8] A. P. Mosk, A. Lagendijk, G. Lerosey, and M. Fink, *Controlling waves in space and time for imaging and focusing in complex media*, Nature Phot. **6**, 283-292 (2012).

[9] J. Aulbach, B. Gjonaj, P. M. Johnson, A. P. Mosk, and A. Lagendijk, *Control of light transmission through opaque scattering media in space and time*, Phys. Rev. Lett. **106**, 103901 (2011).

[10] O. Katz, E. Small, Y. Bromberg, and Y. Silberberg, *Focusing and compression of ultrashort pulses through scattering media*, Nature Phot. **5**, 372-377 (2011).

[11] D. J. McCabe, A. Tajalli, D. R. Austin, P. Bondareff, I. A. Walmsley, S. Gigan, and B. Chatel, *Spatio-temporal focusing of an ultrafast pulse through a multiply scattering medium*, Nature Commun. **2** 447 (2011).

[12] J. H. Park, C. H. Park, H. Yu, Y. H. Cho, and Y. K. Park, *Active spectral filtering through turbid media*, Opt. Lett. **37**, 3261-3263 (2012).

[13] E. Small, O. Katz, Y. Guan, and Y. Silberberg, *Spectral control of broadband light through random media by wavefront shaping*, Opt. Lett. **37**, 3429-3431 (2012).

[14] J. H. Park, C. Park, H. Yu, Y. H. Cho, and Y. K. Park, *Dynamic active wave plate using random nanoparticles*, Opt. Express **20**, 17010-17016 (2012).

[15] Y. Guan, O. Katz, E. Small, J. Zhou, and Y. Silberberg, *Polarization control of multiply-scattered light through random media by wavefront shaping*, Opt. Lett. **37**, 4463-4665 (2012).

[16] R. Fiolka, K. Si, and M. Cui, *Complex wavefront corrections for deep tissue focusing using low coherence backscattered light*, Opt. Express **20**, 16532-16543 (2012).

[17] J. Jang, J. Lim, H. Yu, H. Choi, J. Ha, J. H. Park, W. Y. Oh, W. Jang, S. D. Lee, and Y. K. Park, *Complex wavefront shaping for optimal depth-selective focusing in optical coherence tomography*, Opt. Express **21**, 2890-2902 (2013).

[18] Y. Choi, T. R. Hillman, W. Choi, N. Lue, R. R. Dasari, P. T. So, W. Choi, and Z. Yaqoob, *Measurement of the Time-Resolved Reflection Matrix for Enhancing Light Energy Delivery into a Scattering Medium*, Phys. Rev. Lett. **111**, 243901 (2013).

[19] S.M. Popoff, G. Lerosey, M. Fink, A.C. Boccara, and S. Gigan, *Image transmission through an opaque material*, Nat. Commun. **1**, 81 (2010).

[20] I.M. Vellekoop and C.M. Aegerter, *Scattered light fluorescence microscopy: imaging through turbid layers*, Opt. Lett. **35**, 1245-1247 (2010).

[21] G. Ghielmetti and C.M. Aegerter, *Scattered light fluorescence microscopy in three dimensions*, Opt. Lett. **20**, 3744-3752 (2012).

[22] C. L. Hsieh, Y. Pu, R. Grange, G. Laporte, and D. Psaltis, *Imaging through turbid layers by scanning the phase conjugated second harmonic radiation from a nanoparticle*, Opt. Express **18**, 20723-20731 (2010).

[23] X. Yang, C.L. Hsieh, Y. Pu, and D. Psaltis *Three-dimensional scanning microscopy through thin turbid media*, Opt. Express **20**, 2500-2506 (2012).

[24] J. Bertolotti, E.G. van Putten, C. Blum, A. Lagendijk, W.L. Vos, and A.P. Mosk *Non-invasive imaging through opaque scattering layers*, Nature **491**, 232-234 (2012).

[25] D.B. Conkey, A.M. Caravaca-Aguirre, and R. Piestun *High speed scattering medium characterization with application to focusing light through turbid media*, Opt. Express **20**, 1733-1740 (2012).

[26] I. Freund, M. Rosenbluh, and S. Feng, *Memory effects in propagation of optical waves through disordered media*, Phys. Rev. Lett.**61**, 2328-2331 (1988).

[27] D.L. Fried, *Anisoplanatism in Adaptive Optics*, J. Opt. Soc. Am. 72, 52-61 (1982).

[28] S. Feng, C. Kane, P.A. Lee, and A.D. Stone, *Correlations and Fluctuations of Coherent Wave Transmission through Disordered Media*, Phys. Rev. Lett. **61**, 834-837 (1988).

[29] Z. Yaqoob, D. Psaltis, M.S. Feld, and C. Yang, *Optical phase conjugation for turbidity suppression in biological samples*, Nat. Photonics **2**, 110-115 (2008).

[30] M. Cui, E.J. McDowell, and C. Yang, *An in vivo study of turbidity suppression by optical phase conjugation (TSOPC) on rabbit ear*, Opt. Express **18**, 25-30 (2010).

[31] M. Cui and C. Yang, *Implementation of a digital optical phase conjugation system and its application to study the robustness of turbidity suppression by phase conjugation*, Opt. Express **18**, 3444-3455 (2010).

[32] G. Lerosey, J. de Rosny, A. Tourin, and M. Fink, *Focusing beyond the diffraction limit with far-field time reversal*, Science **315**, 1120-1122 (2007).

[33] M. Fink, *Time reversed acoustics*, Phys. Today **50**, 34-40 (1997).

[34] J.L. Thomas, F. Wu, and M. Fink, *Time reversal focusing applied to lithotripsy*, Ultras. Imag. **18**, 106-121 (1996).

[35] S.M. Popoff, G. Lerosey, R. Carminati, M. Fink, A.C. Boccara, and S. Gigan, *Measuring the Transmission Matrix in Optics: An Approach to the Study and Control of Light Propagation in Disordered Media*, Phys. Rev. Lett. **104**, 100601 (2010).

[36] S.M. Popoff, A. Aubry, G. Lerosey, M. Fink, A.C. Boccara, and S. Gigan, *Exploiting the Time-Reversal Operator for Adaptive-Optics, Selective Focusing, and Scattering Pattern Analysis*, Phys. Rev. Lett. **107**, 263901 (2011).

[37] I.M. Vellekoop, E.G. van Putten, A. Lagendijk, and A.P. Mosk, *Demixing light paths inside disordered metamaterials*, Opt. Express **16**, 67-80 (2008).

[38] G. Ghielmetti and C.M. Aegerter, *Direct imaging of fluorescent structures behind turbid layers*, Opt. Lett. **22**, 1981-1989 (2014).

[39] C. Prada and M. Fink, *Eigenmodes of the time reversal operator:A solution to selective focusing in multiple-target media*, Wave motion **20**, 151-163 (1994).

[40] C. L. Hsieh, Y. Pu, R. Grange, G. Laporte, and D. Psaltis, *Imaging through turbid layers by scanning the phase conjugated second harmonic radiation from a nanoparticle*, Opt. Express **18**, 20723-20731 (2010).

[41] B. Huang, M. Bates, and X. Zhuang *Super-resolution fluorescence microscopy*, Annu. Rev. Biochem. **20**, 993-1016 (2009).

[42] E.W. Forgy *Cluster analysis of multivariate data: efficiency versus interpretability of classifications*, Biometrics **21**, 768-769 (1965).

[43] I.M. Vellekoop *Controlling the propagation of light in disordered scattering media*, PhD thesis (2008).

[44] J. W. Goodman *Statistical optics*, Wiley, New York (2000).

[45] D. Akbulut, T. J. Huisman, E. G. van Putten, W. L. Vos, and A. P. Mosk, *Focusing light through random photonic media by binary amplitude modulation*, Opt. Express **19**, 4017âĂŞ4029 (2011).

[46] I. M. Vellekoop and C. M. Aegerte, *Focusing light through living tissue,*, Proc. SPIE **7554**, 755430 (2010).

[47] M. Cui, *A high speed wavefront determination method based on spatial frequency modulations for focusing light through random scattering media*, Opt. Express **19**, 2989âĂŞ2995 (2011).